NTNU

Norwegian University of
Science and Technology

Fracture Treatment Simulations Using a Modified Discrete Element Model (MDEM)

Andreas Baastad

Petroleum Geoscience and Engineering
Submission date: June 2016
Supervisor: Andreas Bauer, IPT

Norwegian University of Science and Technology
Department of Petroleum Engineering and Applied Geophysics

Abstract

Hydraulic fracturing is a widely used well-stimulation technique and one of the primary engineering tools for enhanced well productivity. To improve the understanding of how untouched rock mass reacts to stimulation, SINTEF Petroleum Research has developed a simulator called Modified Discrete Element Method (MDEM). In this thesis, MDEM simulations are compared to literature and established truths to better understand the mechanisms in the reservoir. The main focus will be on investigating the effects of natural fractures and shear-dilation during fracture treatments. Both features are known to increase the stimulated area. After fracture treatments, shear-dilation can also help in maintaining the enhanced conductivity. Numerical studies have been conducted to look at fracture propagation in naturally fractured reservoirs and the final effect of shear-dilation on fracture treatments. Also, an attempt was done to mimic altered fluid viscosity in the simulator, and fall-off tests were carried out to investigate the possibility of using MDEM to estimate fracture properties. The direction of natural fractures, both on a global (meters) and a local (centimeters) scale, showed to have great impact on the induced fractures' half lengths. Natural fractures must therefore be taken into account when fracture stimulations are planned. Shear-dilation showed little relative effect on fracture aperture during injection, but was found to be of great importance after the treatment was ended and the fractures had closed.

Sammendrag

Hydraulisk oppsprekking er en mye brukt stimuleringsteknikk og et av hovedverktøyene for økt produktivitet. For å bedre forståelsen for hvordan urørte formasjoner reagerer på stimulering har SINTEF Petroleumsforskning utviklet en simulator kalt Modified Discrete Element Method (MDEM). I denne oppgaven er MDEM-simuleringer sammenlignet med litteratur og etablerte sannheter for å bedre forstå mekanismene i reservoaret. Hovedfokuset vil være å undersøke effektene av naturlige sprekker og skjær-utvidelse under oppsprekkingsbehandling. Begge egenskapene er med på å øke det stimulerte området. Etter oppsprekkingsbehandlingen kan skjær-utvidelse også hjelpe til å vedlikeholde den økte konduktiviteten. Numeriske studier har blitt gjennomført for å se på oppsprekkingspropagering i naturlig oppsprukne reservoarer og den endelige effekten skjær-utvidelse har på oppsprekkingsbehandlinger. Det har også blitt gjort et forsøk på å etterligne en endret fluidviskositet i simulatoren, og trykkfalltester har blitt utført for å utforske mulighetene for å bruke MDEM til å estimere sprekkegenskaper. Retningen på naturlige sprekker, både i global (meter) og lokal (centimeter) skala, viste seg å ha stor innvirkning på de induserte sprekkenes halvlengde. Naturlige sprekker må derfor tas med i beregningen når oppsprekkingsbehandlinger blir planlagt. Skjær-utvidelse viste liten relativ innvirkning på sprekkåpning under injeksjon, men hadde stor betydning etter behandlingen var ferdig og sprekkene hadde lukket seg.

Acknowledgements

First of all, I would like to thank my supervisor, Andreas Bauer, for the guidance he has given me during the thesis. I would also like to thank PhD student, Mats Rongved, for teaching me MDEM and helping me do some of the simulations. Idar Larsen at SINTEF deserves a big thanks for his expert advices whenever I needed some help.

I also express my sincere gratitude to all my classmates who have helped me through the last five years. Last but not least, I want to thank my parents for their moral and financial support during my studies.

Table of contents

List of figures

List of tables

1 Introduction

Fracking has come a long way since 1857 when Preston Barmore lowered gunpowder into a well and sat off an explosion to fracture the formation and increase the production rate (Morton, 2013). The idea behind, and the ultimate goal of fracking, is still the same, but since the first commercially applied hydraulic fracturing processes was conducted in the 1940's (Clark, 1949), pressurized fluid has been the preferred fracturing agent. More recent developments are the use of fractures in horizontal wells and tight formations. The new application of fracking has revolutionized the petroleum industry and reshaped the global energy landscape. The amount of oil from fractured wells has increased from 2% to more than half of all U.S. oil output in the last six years, and there are now 300,000 fracking wells, producing 4.3 million barrels of oil per day (Egan, 2016). Today, hydraulic fracturing has become one of the primary engineering tools for improving well productivity (Smith and Shlyapobersky, 2000: 1).

Like so much else, if it's used without care fracturing may also have adverse effects. The fractures can end up growing into the cap rock and break the sealing of the reservoir, or into the water leg and cause production of water. Even though today's fracturing processes are done under more controlled conditions than in 1857, the fractures still can't be completely controlled. Ultimately, the nature decides. To better understand fracture mechanics, more reliable fracture simulations tools, that take the complexity of hydraulic fracturing into account, are needed. SINTEF Petroleum Research has developed a simulator based on numerical modelling called Modified Discrete Element Method (MDEM). Like the name implies, MDEM is a modification of the discrete element method (DEM). In this new approach, MDEM behaves similar to the finite element method (FEM) initially. It starts to behave like DEM only after rock failure. This way some of FEM's benefits are maintained, while fracture propagation is handled by DEM, a less complicated numerical technique. The goal of this thesis is to learn more about fracture mechanics through comparison of literature and results obtained from MDEM simulations. The main focus will be on investigating the effects of natural fractures and shear-dilation.

Chapter 2 will give an introduction to relevant theoretical concepts. The key topics are hydraulic fracturing and numerical modeling. The concepts introduced are chosen based on the simulations done during the thesis. An attempt is done to easily explain how MDEM works.

From Chapter 3 and out, it is less about theory and more about the simulations. In Chapter 3, the numerical scheme and physical properties of the formation are presented, together with an overview of the different simulations. Results and discussions are presented in Chapter 4, before the thesis is concluded in Chapter 5. Further work is suggested in Chapter 6.

2 Theoretical Concepts – An Introduction to MDEM and Hydraulic Fracturing

2.1 Basics of hydraulic fracturing

Hydraulic fracturing is a widely used well-stimulation technique and one of the primary engineering tools for improving well productivity (Smith and Shlyapobersky, 2000: 1). To create conductive channels in the reservoir, the rock is fractured by pressurized liquid pumped down the well. Fracturing fluid is pumped into the well faster than the fluid can escape into the formation. As more fluid is pumped into a limited volume, the pressure rises until something breaks. The weakest material is usually the formation, and when it eventually breaks, a fracture is created out from the wellbore. The process can also open up pre-existing natural fractures present in the formation. The fractures help improving the productivity by (Smith and Shlyapobersky, 2000: 1)

- creating a conductive path through the damaged zone near the wellbore,
- extending the conductive network deeper into the reservoir, and
- placing the channels such that fluid flow in the reservoir is altered.

Bypassing the damaged zone helps a permeable reservoir return to its "initial" productivity. During drilling, plugging of pores by invasion of fines or chemical incompatibility between drilling fluid and the formation can result in reduced conductivity (Smith and Shlyapobersky, 2000: 4). The hydraulically induced fractures create a new contact between the wellbore and the undamaged rock, thus restoring its natural permeability. The ability to create deep conductive networks into the reservoir has opened up for hydrocarbon resources that previously were looked at as inaccessible. In low permeability formations like tight oil and gas (permeability less than 0.1 millidarcy), the fractures stimulate productivity beyond the natural level and create the permeability necessary for the formation fluids to flow. The matrix permeability is not altered, but the increased flow area the fractures create between the formation and the wellbore increases the secondary permeability. Altering the fluid flow in a reservoir by the use of hydraulic fracturing makes a great reservoir management tool. Reservoirs can be depleted with fewer wells and big money can be saved.

2.1.1 Fracture mechanics and failure criteria

The increased down-hole pressure during hydraulic fracturing results in tensile failure of the rock. Tensile failure occurs when the effective tensile stress in the rock exceeds a critical limit called tensile strength, denoted by T_0. The tensile strength is a characteristic property of the rock, varying from sample to sample. The failure criterion is given as (Fjær et al., 2008: 60)

$$\sigma' = -T_0, \qquad \text{Eq. 2.1}$$

where σ' is the effective tensile stress. Compared to normal stress, the effective stress also accounts for pore pressure:

$$\sigma' = \sigma - p_f. \qquad \text{Eq. 2.2}$$

Here, σ is the stress, and p_f is the pore pressure.

Fracture initiation

During well operations, the tensile fractures first start to form at the borehole wall. If the well pressure differs from the formation pressure, it may cause large stress deviations in the formation close to the borehole. In a borehole drilled along a principal stress direction in an impermeable formation, the lowest tangential stress, $\sigma_{\theta,min}$, is given as (see Fjær et al. (2008: 145-149) for derivation)

$$\sigma_{\theta,min} = 3\sigma_h - \sigma_H - p_w, \qquad \text{Eq. 2.3}$$

where σ_h and σ_H is the minimum and maximum principal stresses perpendicular to the well, respectively, and p_w is the well pressure. The lowest value of σ_θ occurs in the direction of the maximum principal stress where $\theta = 0$. The fracture will thus grow perpendicular to the minimum principal stress. Physically, this is explained by the tendency of a fracture to grow in the direction of least resistance. For a fracture growing perpendicular to the minimum principal stress, the minimum principal stress is the main force that needs to be overcome. In a rock without natural fractures, the minimum principal stress is the dominant parameter controlling the fracture geometry (Smith and Shlyapobersky, 2000: 9).

The borehole pressure needed to initiate fractures is different in permeable and impermeable formations. If the failure criterion in Eq. 2.1 and Eq. 2.2 is combined with Eq. 2.3, the criterion in an impermeable formation becomes (Fjær et al., 2008: 159)

$$p_{w,max}^{frac} = 3\sigma_h - \sigma_H - p_f + T_0. \quad \text{Eq. 2.4}$$

In a permeable formation, the pore pressure near the wellbore equals the well pressure. The altered pore pressure in permeable formations induces changes in the total stresses, and the minimum tangential stress becomes

$$\sigma_{\theta,min} = 3\sigma_h - \sigma_H - p_w + 2\eta(p_w - p_{f0}), \quad \text{Eq. 2.5}$$

where η is the poroelastic stress coefficient (see Fjær et al. (2008: 141) for mathematical description) and p_{f0} is the in-situ pore pressure. The criterion for fracturing along the wellbore wall then becomes

$$p_{w,max}^{frac} = \frac{3\sigma_h - \sigma_H - 2\eta p_{f0} + T_0}{2 - 2\eta}. \quad \text{Eq. 2.6}$$

Fracture propagation

For further fracture growth after fracture initiation, the stress concentration at the fracture tip has to overcome the fracture toughness. The stress concentration around the fracture tip can be calculated by the following equation (Bauer, 2016):

$$\sigma_{ij}(r,\theta) = \frac{K}{\sqrt{2\pi r}} f_{ij}(\theta). \quad \text{Eq. 2.7}$$

K is the stress-intensity factor, and r is the radial distance from the fracture tip in the direction of θ. f_{ij} is a function depending on the crack geometry and loading conditions. For tensile fractures, K is proportional to the fracture pressure, p_{frac}, and the fracture length, L, like (Bauer, 2016)

$$K \propto \left(p_{frac} - \sigma_3\right) * \sqrt{L}. \quad \text{Eq. 2.8}$$

Fracture propagation occurs when K equals the critical fracture toughness, K_c. From the equation it is clear that σ_3 is the limiting factor. In addition, it can be seen how the length of the fracture helps its propagation. The fluid in the fracture works as a wedge, and the longer the wedge gets, the easier it is to open the fracture further. Frictional losses in fractures partly counteract the wedge effect. As the fracture increases in length, the frictional losses increases, and p_{frac} decreases.

2.1.2 Fluid leak-off in fractured wells

Fracture growth results in a larger fracture volume. As a consequence, the amount of fluid in the well obviously has to increase to maintain the well pressure above the fracture propagation pressure. The fluid injected from the surface is not the only factor effecting the amount of fluid in the well; in permeable formations some fluid will also leak off into the formation. It is the sum of injected and lost fluid that determines the well pressure. For a fracture to propagate, the net flow of fluid into the well must be positive.

Fracture growth exposes the injected fluid to new areas of formation, and as a result, the rate of fluid leak-off increases. As introduced by R.D. Carter (Howard and Fast, 1957), the leak-off rate, q_L, from an element, A, of the fracture area can be expressed as (Smith and Shlyapobersky, 2000: 2)

$$q_L \approx \frac{2C_L A}{\sqrt{t-\tau}}, \quad \text{Eq. 2.9}$$

where C_L is the fluid-loss coefficient, t is the time since injection started, and τ is the time when element A of the fracture was opened. From the equation one can see that the highest leak-off rate always will be at the fracture tip. The moment new formation is opened to the fracture fluid, $\tau = t$ $(t - \tau = 0)$, and q_L at the fracture tip is instantly infinite (Smith and Shlyapobersky, 2000: 2). With time, the $\sqrt{t-\tau}$-term for a specific element of the fracture area increases, and q_L will decrease. As a fracture propagates, larger areas are opened to leak-off, and the leak-off rate increases. With a constant injection rate, the net fluid flow will decrease.

Well pressure will build up slower, and the fracture propagation pressure will be reached later. The result is a reduced fracture propagation rate. The fracture will eventually be more or less stable.

Other parameters also affect the leak-off rate. The fluid-loss coefficient in Eq. 2.9 varies from well to well and depends on many factors, including the injection pressure and the viscosity and the relative permeability of the fracturing filtrate (Shapiro, 2015: 166; Guo and Liu, 2014). Fluid will leak off easier with lower viscosity and a more permeable formation. The leak-off results in an increasing pressure and a decreasing pressure gradient around the fracture. With time, more and more fluid enters the formation and the pore pressure rises. In addition, a filter cake often starts to form on the borehole wall. As a result, it will become increasingly more difficult for new fluids to enter the formation. This is also taken into account in the $\sqrt{t-\tau}$-term.

2.1.3 Shear-dilation in rough walled fractures

The fracture walls in a failed rock are seldom completely smooth. In a fracture, the asperity height distribution, the asperity slopes, and the correlation distances vary depending on the rock and its grain size (Odling, 1997: 291). To characterize a fracture wall through one parameter, the 'joint roughness coefficient' (JRC) based on friction characteristics was introduced by Barton and Choubey (1977). Later, methods directed at quantitative descriptions of fracture surface geometry have been introduced (e.g. Tse and Cruden (1979)).

The roughness of a fracture affects the fluid flow in different ways. Asperities create friction and can cause changes in the flow regime. They can also increase the aperture of a fracture, hence increase the permeability. Three contributions are known to affect the mechanical (geometrical) aperture of a rough-walled fracture (Lavrov et al., 2016):

- the initial aperture,
- the aperture growth caused by normal opening, and
- the aperture growth caused by shear-induced dilation.

The last point – shear-induced dilation – relies on the presence of asperities on the fracture surface and shear movement within the fracture.

From shear movement to increased aperture

It is not that easy to understand how shear displacement, u_s, can cause increased aperture of a fracture. In a fracture with parallel smooth walls, the aperture would be zero as long as $u_n = 0$, even when $u_s \neq 0$. In reality, where fracture walls have asperities, it is different. During shear movement, the asperities sliding over one another causes the fractures to open (see Figure 2.1). This is confirmed by experiments (Mitani et al., 2005; Mehrishal and Sharifzadeh, 2012). The experiments show how the hydraulic aperture of a fracture increases with u_s, asymptotically approaching some value, $\Delta w_{(s)max}$. The maximum value, $\Delta w_{(s)max}$, is physically explained by the maximum height of the asperities (see Figure 2.1c). A schematically illustration of the behavior is shown in Figure 2.2.

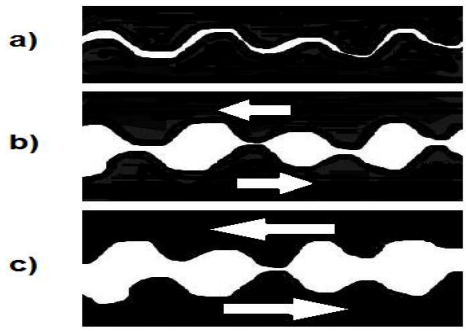

Figure 2.1. A fracture during the shear-dilation process: a) a fracture has been created, b) the fracture opens as shearing causes asperities to bump into each other, and c) the asperities no longer touch each other and $\Delta w_{(s)max}$ is reached. Further shear movement has no effect on the aperture.

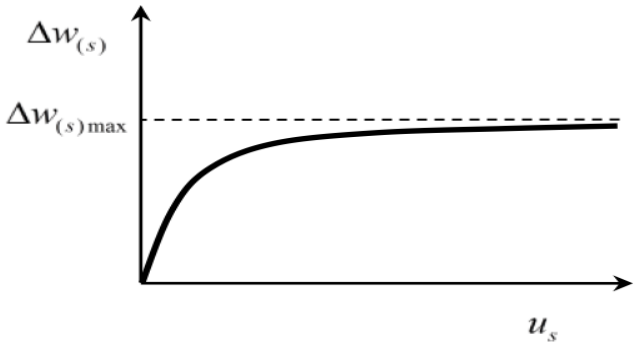

Figure 2.2. Shear displacement's contribution to hydraulic aperture (Lavrov et al. (2016) based on findings by Mitani et al. (2005)).

2.1.4 Effects of natural fractures

In brittle formations, natural fractures are frequently seen, but their orientations and persistence in situ are often unknown. The uncertainty is a major reason for predictive difficulties in hydraulic fracture behavior (Dusseault, 1989).

Fracture patterns

Because the matrix has a significantly larger fracture resistance than a natural fracture, hydraulic fractures are likely to initiate in some other direction than perpendicular to σ_3 if a natural fracture intersects the borehole. In such a case, the fracture initiation pressure will therefore reflect a different tangential stress than the one usually calculated. In further induced fracture propagation, the tip processes are important at a local scale. When a natural fracture is opened, the shear stress resulting from anisotropic stress fields must be relieved because the fluid in the fracture cannot withstand shear force. Because of the resulting lateral movement, loading distortion creates varying stress fields in the ancillary natural fractures. The effect is shown in the magnified area in the upper, left corner of Figure 2.3. The fracture follows the path of least compressive strength and will thus turn. The process of lateral movement, loading distortion, and fracture turning continues and keeps the fracture propagating in the direction perpendicular to σ_3 on a global scale (lower part of Figure 2.3). As a general rule, hydraulic fractures follow natural fractures locally, but globally, they are normal to σ_3 (Dusseault, 2015: 64-65; Dusseault, 1989).

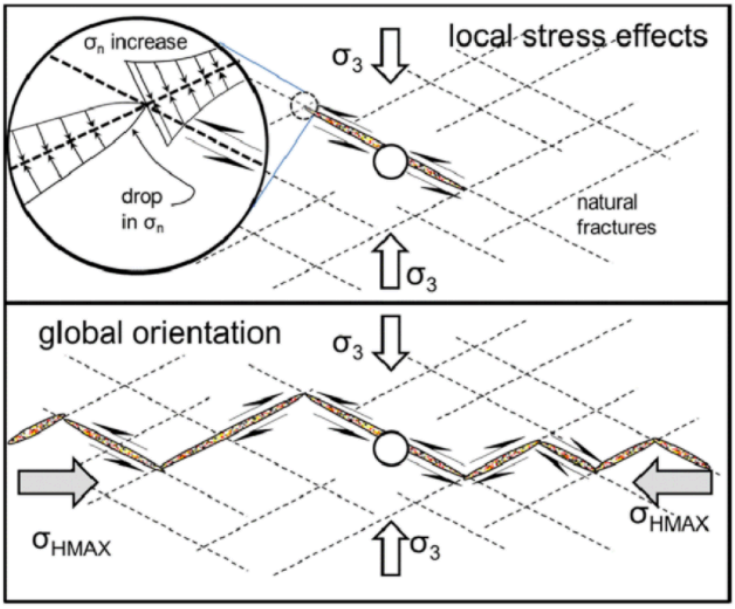

Figure 2.3. The mechanics behind fracture growth in natural fractured formations. Induced local fracture directions changes as a function of orientation and scale (Dusseault, 2015: 65).

Increased stimulated volume

The shear-dilation phenomenon presented in Section 2.1.3 does not only apply to induced fractures. In natural fractured formations, also detached natural fractures can be affected (Dusseault, 2015: 65-67). Due to leak-off from the wellbore and associated fractures, the formation pressure increases, and effective stresses decreases. If the slip criterion of a natural fracture is satisfied, shear displacement occurs to relieve the shear stresses. As explained in the previous section, shear displacement pushes the rough fracture walls apart, leaving remnant conductivity along the fracture plane (see Figure 2.4). The remnant conductivity contributes to the overall flow enhancement of the hydraulically fractured formation, and leads to the concept of "stimulated volume". After a hydraulic fracture treatment, there is a central zone of hydraulic fractures and a surrounding zone of enhanced conductivity due to shear-dilation in natural fractures. The concept is illustrated in Figure 2.5 and is evidenced by microseismic events (Dusseault, 2015: 67).

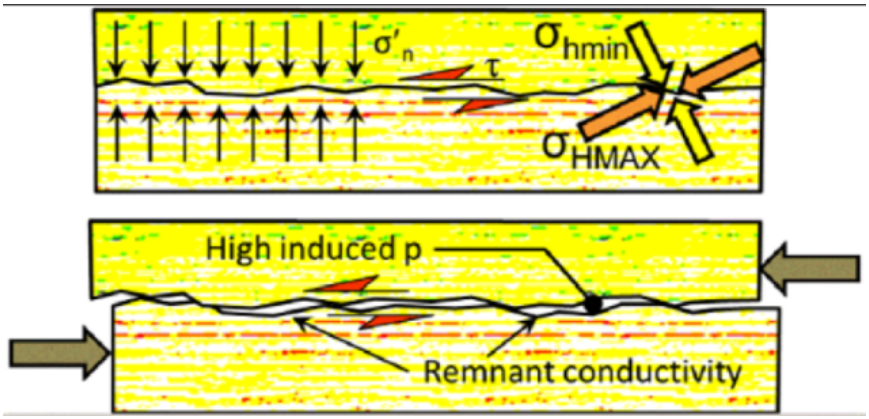

Figure 2.4. Shear-dilation in a separate, closed natural fracture (Dusseault, 2015: 66).

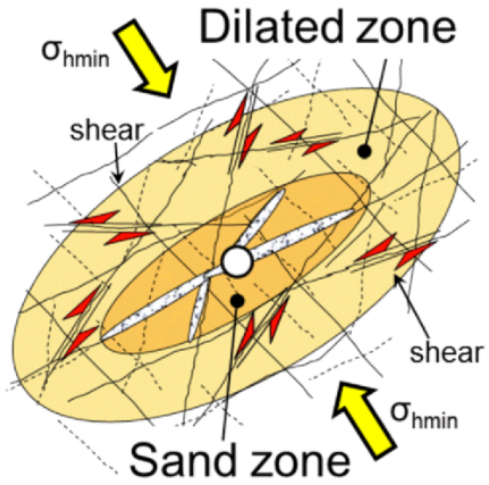

Figure 2.5. Illustration of the concept "stimulated volume". The central zone around the borehole and associated hydraulic fractures is surrounded by a zone where shear-dilation of natural fractures has enhanced the conductivity (Dusseault, 2015: 67).

2.1.5 Rheology of fracturing fluids

Rheology is the study of the flow of matter (Saboo and Kumar, 2016). If flowing fluids are part of a simulation, the rheological properties are of huge importance. An essential property, with a potentially significant impact on the results, is viscosity. In petroleum engineering one usually talks about the dynamic viscosity of a fluid, defined as "the resistance to shearing flows". A lot of effort has been put in to designing the optimal fracturing fluid rheology. To minimize leak-off, expensive additives have been used to elevate the viscosity (Palisch et al., 2008). For effective placement of proppants, complex fracturing fluid systems are engineered to change

viscosity during its journey from the surface to the fractures and then again during fracture clean up (Mayerhofer et al., 1997).

Viscosity

The nature of viscosity can best be described through the method used to measure it (see also Figure 2.6). Consider two plates of area A, separated by a distance L of a fluid. If the lower plate is kept at rest, a constant force F is required to move the upper plate at a constant velocity V. The magnitude of the force F has been found experimentally to be given by (Bourgoyne Jr. et al., 1986: 131)

$$\frac{F}{A} = \mu \frac{V}{L}. \qquad \text{Eq. 2.10}$$

The term on the left-hand side of the equation, F/A, is called shear stress and is denoted by τ. The velocity gradient V/L is an expression of the shear rate, $\dot{\gamma}$. Eq. 2.10 can then be written as

$$\tau = \mu\dot{\gamma}, \qquad \text{Eq. 2.11}$$

where μ is known as the viscosity of the fluid. Viscosity is expressed in poise, and a poise equals 1 dyne-s/cm^2 or 1 g/cm*s. In the drilling industry, viscosity generally is expressed in centipoise (cP) (Bourgoyne Jr. et al., 1986: 132).

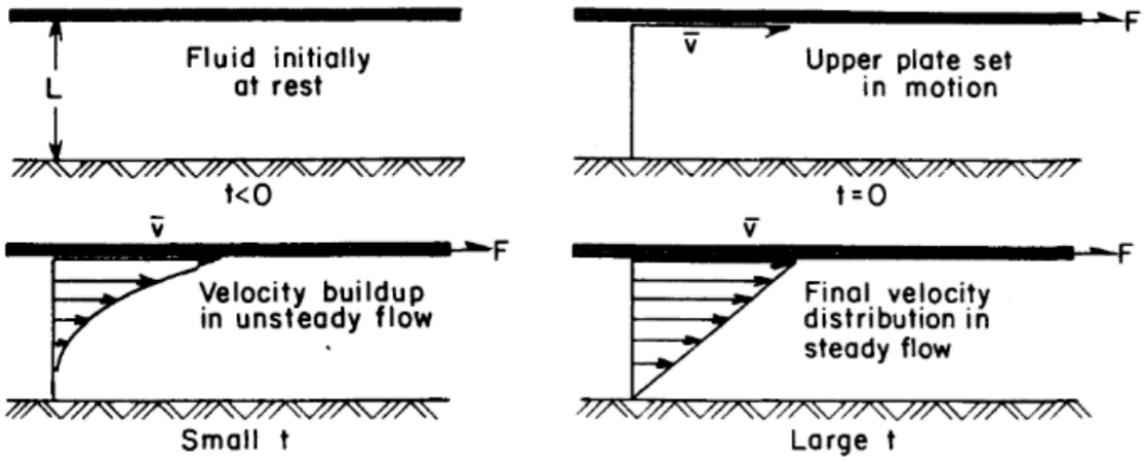

Figure 2.6. Viscosity measurement. Viscosity is found by measuring the constant force needed to move a plate at constant velocity (Bourgoyne Jr. et al., 1986: 132).

Newtonian fluids

For some fluids, e.g. water, gases, and high gravity oils, the shear stress is directly proportional to the shear rate. For these fluids, the viscosity term in Eq. 2.11 will stay constant, and a change in shear rate will only result in a equal relative change in shear stress. The linear relationship is shown in Figure 2.7. Fluids experiencing this behavior are called Newtonian fluids. It is worth mentioning that the linear relation only is valid for laminar flow.

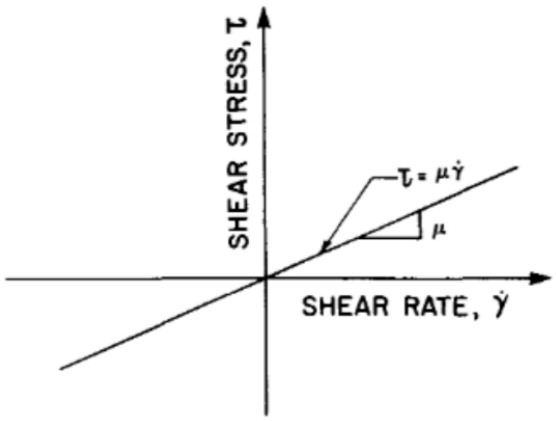

Figure 2.7. Shear rate vs. shear stress for a Newtonian fluid (Bourgoyne Jr. et al., 1986: 132).

Non-Newtonian fluids

The viscosity of most drilling fluids can't be described by one, single value. Instead, the apparent viscosity changes depending on the shear rate and the fluid's shear rate history. Fluids without a direct proportionality between shear rate and shear stress are called non-Newtonian fluids. If the viscosity decreases when the shear rate increases, the fluid is pseudoplastic (see Figure 2.9). It is dilatant if the viscosity increases with increasing shear rate. If a fluid is shear-time-dependent, it is thixotropic if the viscosity decreases with time after the shear rate is increased and rheopectic if the viscosity increases with time. Drilling fluids are generally pseudoplastic and thixotropic.

Two rheological models are commonly used to approximate the pseudoplastic behavior of fluid: the Bingham plastic model and the power-law model (Bourgoyne Jr. et al., 1986: 133). Thixotropic behavior is not modeled mathematically. In most cases, it is satisfactory to neglect thixotropy, but large velocity changes in the flow system can cause significant errors.

Bingham plastic fluids

A Bingham plastic fluid behaves like a solid when it is not in motion. A minimum shear stress, τ_y, also known as the yield point, must be applied before it starts to flow. After the yield point is exceeded, the shear stress will change proportionally to the shear rate. The constant of proportionality is called plastic viscosity, μ_p. The Bingham plastic model is defined by (Bourgoyne Jr. et al., 1986)

$$\tau = \mu_p \dot{\gamma} + \tau_y \ ; \quad \tau > \tau_y \qquad \text{Eq. 2.12}$$

$$\dot{\gamma} = 0 \ ; \quad -\tau_y \leq \tau \leq +\tau_y \qquad \text{Eq. 2.13}$$

$$\tau = \mu_p \dot{\gamma} - \tau_y \ ; \quad \tau < -\tau_y \qquad \text{Eq. 2.14}$$

Figure 2.8 shows a graphical representation of the yield point and the linear relation between shear rate and shear stress after the yield point has been exceeded.

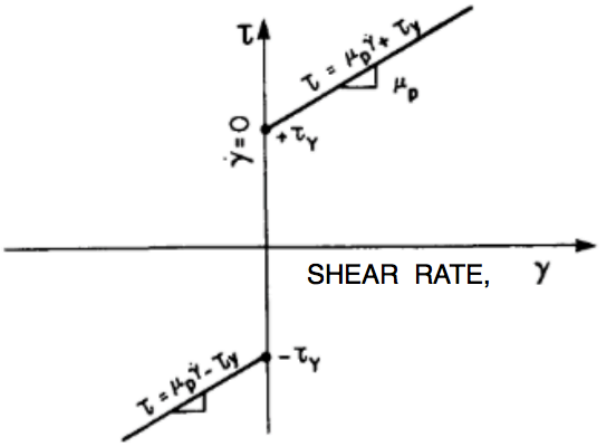

Figure 2.8. Shear rate vs. shear stress for a Bingham plastic fluid (Bourgoyne Jr. et al., 1986: 134).

For drilling muds, a high yield point helps to improve the cuttings removal. Experiments have shown that the slip velocity of cuttings are reduced by an increased yield value (Hopkin, 1967). At the same time, the yield point can't be too high because of the excessive pump pressure needed to initiate mud flow.

Power-law fluids

Power-law fluids are generally defined as fluids that change viscosity as the share rate changes, i.e. pseudoplastic and dilatant fluids. The power-law model is mathematically defined by (Bourgoyne Jr. et al., 1986: 134)

$$\tau = K|\dot{\gamma}|^{n-1}\dot{\gamma}. \qquad \text{Eq. 2.15}$$

K is called the consistency index of the fluid. The parameter n is usually called the flow behavior index. By varying n, the model can represent a dilatant fluid ($n > 1$), a Newtonian fluid ($n = 1$), or a pseudoplastic fluid ($n < 1$).

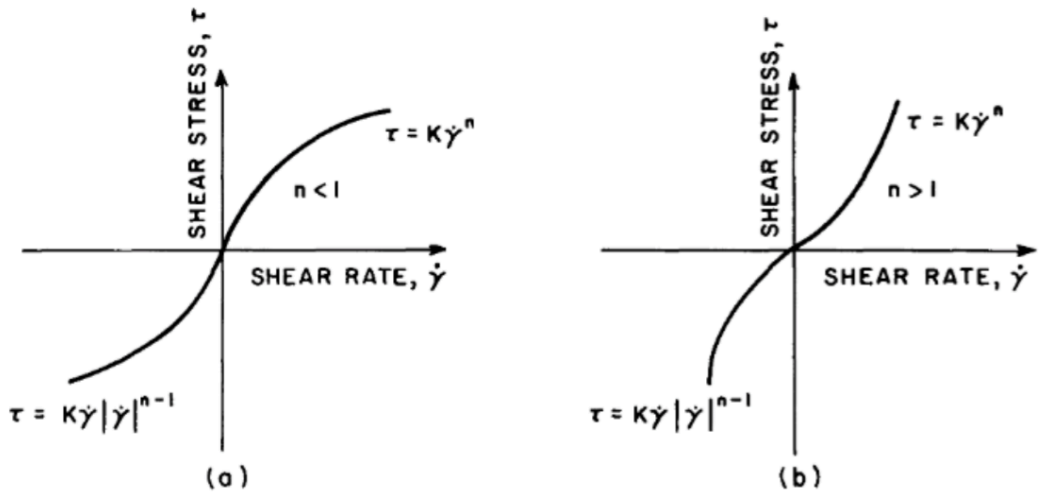

Figure 2.9. Shear rate vs. shear stress for (a) pseudoplastic and (b) dilatant power-law fluids (Bourgoyne Jr. et al., 1986: 135).

Water-fracs

The importance of rheology in fracturing fluids is mainly related to effective placement of proppants. The need of proppants to keep the fractures open and maintain conductivity after end of injection was considered an established truth. In addition to the naturally occurring sand grains, specially engineered proppants like resin-coated sand and high-strength ceramic materials have been used. The treatment process is complex, the fracturing fluid is expensive, and it can damage the formation. In the last decades a new approach called water-fracs has emerged. Instead of using proppants, the new idea is to rely on shear-dilation and let asperities keep the fractures open. Since proppant transport no longer is an issue, high viscosity is

superfluous, and regular water can be used. Some even like to "slicken" the water to reduce friction losses in pipes (Palisch et al., 2008). The new way of thinking started after Mayerhofer et al. (1997) purported "we don't need no proppants". The paper showed promising results from water-fracs and presented the hypothesis based on shear-dilation. A more comprehensive set of production comparisons, that concluded water-fracs to be an accepted and successful fracturing technique, were published a year later (Walker et al., 1998). Schein (2005) estimated that more than 30% of all fracture treatments in the U.S. in 2004 were done with water-fracs.

2.1.6 Accessing information about fractures through fall-off curves

It is impossible to know exactly how fractures thousands of meters below the Earth's surface behaves. A visual look or direct measurements are hard or impossible to obtain, and the complexity and number of variables are too large to come up with exact answers based on models and calculations. Numerical models try to come up with predictions, but in the end, it is all based on assumptions. There are, however, ways to estimate many of the fracture properties based on indirect measurements. During hydraulic fracture treatment, a cheap and easy way to access information about the fractures is through a fracture injection/fall-off test (schematically described in Figure 2.10). A fall-off test is the exact opposite of a build-up test; instead of measuring the increasing well pressure after a given time of production, the decreasing well pressure after injection is measured. The fluid leak-off during the injection phase causes increased pressure around the wellbore and the associated fractures. At shut-in, the pressure differential between the fracture and the undisturbed reservoir has been altered (Newendorp and Menzie, 1965). The pressure dissipation in the charged portion of the formation and the resulting pressure decay in the well are what is being measured.

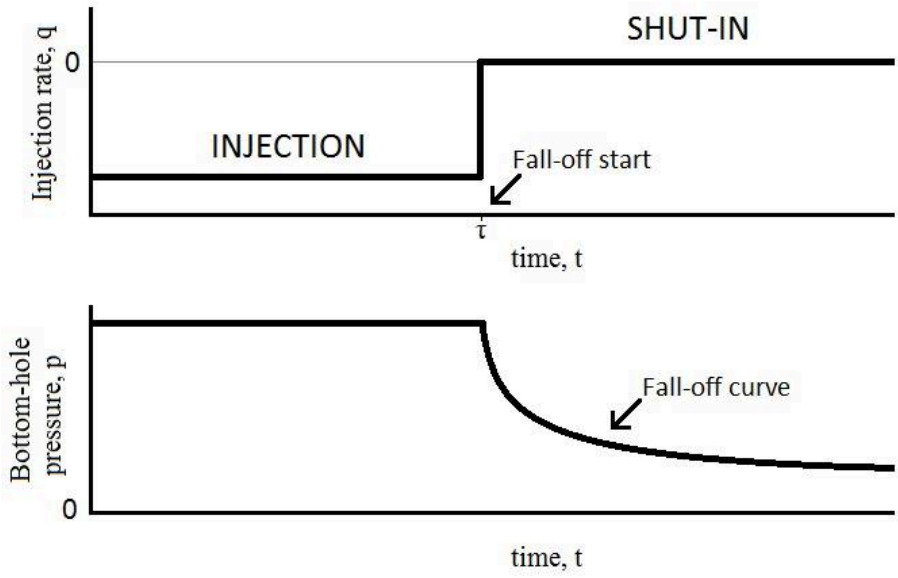

Figure 2.10. Schematic representation of a fracture injection/fall-off test. After the well is shut-in, the bottom-hole pressure starts to decrease.

Factors affecting the fall-off curve

The well pressure, as all other pressures, is a function of temperature, volume, and mass. If the temperature change is neglected, there are two remaining variables during a fall-off test: the amount of fluid and the volume it is kept within. The amount of fluid in the well depends on the leak-off rate, and factors affecting the leak-off rate has been discussed in subchapter 2.1.2 (flow area, viscosity, permeability and pressure difference). The volume varies with the volume of open fractures. As fluid leaks off into the formation, the pressure decreases. Eventually fracture closure pressure is reached, and the fractures start to close. Closed fractures result in less volume. This way the pressure is maintained for longer. Before complete closure of the fractures, the well pressure, p_w, is governed by the gradual loss of hydraulic fracture width, $\overline{w}$ (Marongiu-Porcu et al., 2011)

$$p_w = p_c + S_f \overline{w}, \qquad \text{Eq. 2.16}$$

where p_c is the fracture closure pressure and S_f is the fracture stiffness. From the equation, one can see how the well pressure before fracture closure will fall more rapidly in stiff fractures because the fractures are kept open for longer.

Fracture property estimation through fall-off curves

The behavior of fall-off curves (the pressure plot after shut-in in Figure 2.10) can give information about factors affecting it. If a well is fractured during the injection phase, the fall-off curve will start at a pressure equal to the fracture propagation pressure. With time, the well pressure will approach the initial formation pressure (unless the whole reservoir has been charged). The period in between – the fall-off period – is more complex and harder to interpret, but it can give lots of information about the fracture, e.g. reservoir flow capacity (Newendorp and Menzie, 1965; Nowak and Lester, 1954), fracture closure pressure, fracture length and width, fluid efficiency, leak-off coefficient, and time for the fracture to close (Nolte, 1979; Nolte, 1986; Nolte, 1988; Marongiu-Porcu et al., 2011).

Nolte (1979) introduced the dimensionless g-function, $g(\Delta t, \alpha)$, to estimate the fracture closure pressure, p_c. Before fracture closure the well pressure, p_w, decreases linearly with the g-function like

$$p_w = b_N + m_N g(\Delta t_D, \alpha). \qquad \text{Eq. 2.17}$$

When all fractures are closed, p_w departs from the linear trend (Valko and Economides, 1997). The behavior is illustrated in Figure 2.11. A more recent approach (Marongiu-Porcu et al., 2011) uses the slope of the fall-off pressure derivative. As shown in Figure 2.12, a 3/2 slope will develop on a log-log plot during fracture closure. After fracture closure, the slope deviates and enters the after-closure pseudolinear flow regime seen by a ½ slope.

Marongiu-Porcu et al. (2011) also came up with new methods to estimate m_N and b_N, based on dimensionless shit-in time, Δt_D, superposition time, τ, and pressure derivative, $\Delta p'$. The parameters are given by

$$\Delta t_D = \frac{\Delta t}{t_e}, \qquad \text{Eq. 2.18}$$

$$\tau = \frac{t_e + \Delta t}{\Delta t}, \qquad \text{Eq. 2.19}$$

$$\Delta p' = \frac{dp}{d \ln \tau'}, \quad \text{Eq. 2.20}$$

where t_e is the time of shut-in, and Δt is the time since shut-in. m_N and b_N are then given as

$$m_N = \frac{\Delta p'}{2\Delta t_D^{\frac{5}{2}} \tau (1 - \tau^{\frac{1}{2}})}, \quad \text{Eq. 2.21}$$

$$b_N = p_w - m_N \frac{4}{3} \Delta t_D^{\frac{3}{2}} \left(\tau^{\frac{3}{2}} - 1 \right). \quad \text{Eq. 2.22}$$

To calculate m_N and b_N, the values at fracture closure are used. For 2D KGD-geometry of the fractures, the following equations can be used to calculate leak-off coefficient, C_L, fracture extent, x_f, fracture width, $\overline{w_e}$, and fluid efficiency, η_e:

$$C_L = \frac{\pi x_f}{2\sqrt{t_e} E'} (-m_N) \quad \text{Eq. 2.23}$$

$$x_f = \sqrt{\frac{E' V_i}{\pi h_f (b_N - p_c)}} \quad \text{Eq. 2.24}$$

$$\overline{w_e} = \frac{V_i}{x_f h_f} - 2.956 C_L \sqrt{t_e} \quad \text{Eq. 2.25}$$

$$\eta_e = \frac{\overline{w_e} x_f h_f}{V_i} \quad \text{Eq. 2.26}$$

In KGD-geometry the height of the fractures is assumed equal all the way to the tip of the fracture. The fracture opening at the wellbore is assumed rectangular. The same geometry is used in MDEM.

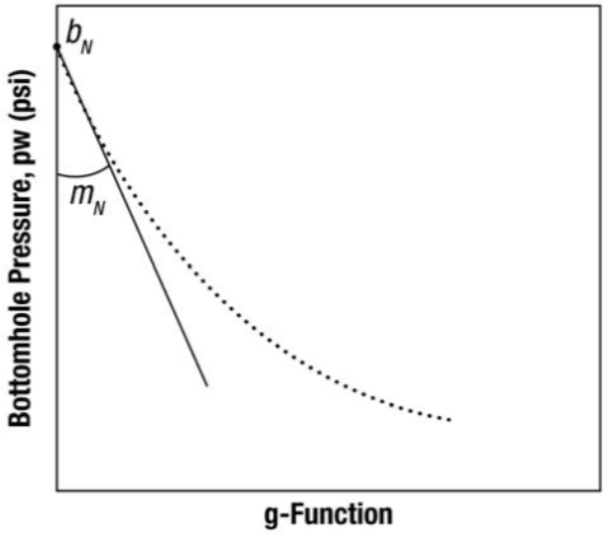

Figure 2.11. Fracture closure pressure determined by the g-function. The well pressure decreases linearly with the g-function until the fractures are closed (Marongiu-Porcu et al., 2011).

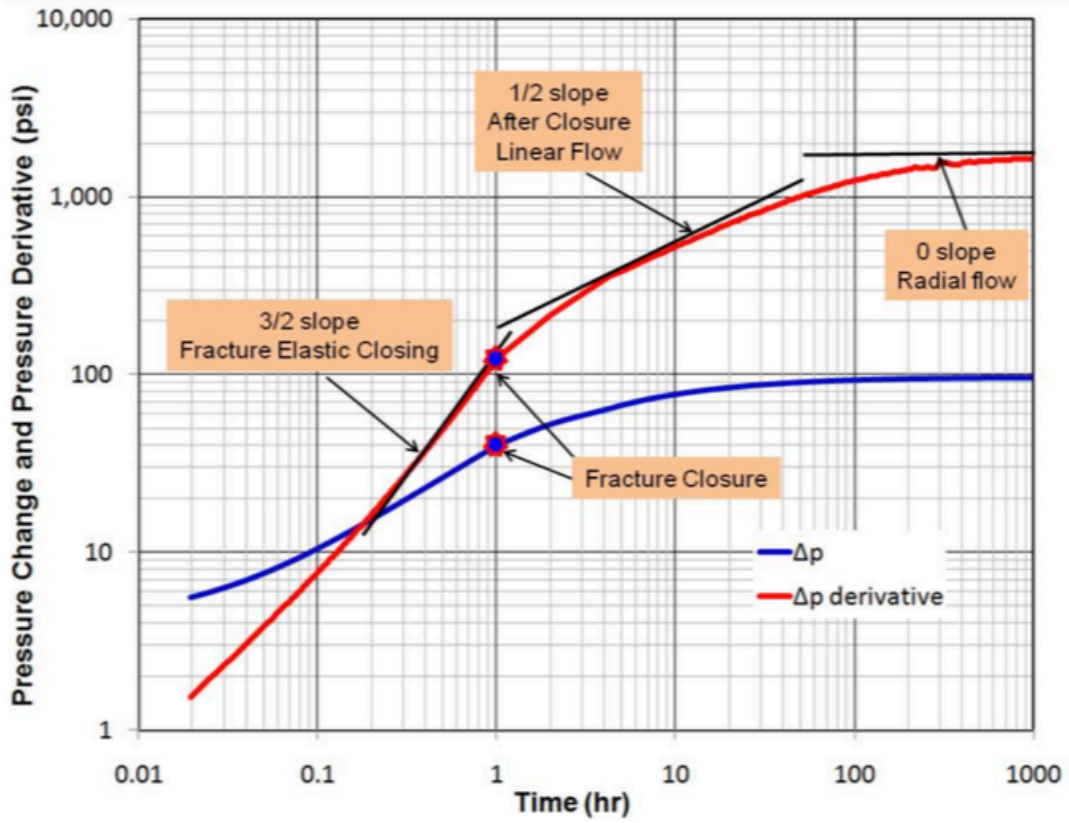

Figure 2.12. Determination of fracture closure pressure through the slope of the fall-off pressure derivative. The graph deviates from the 3/2 slope after the fractures have closed (Marongiu-Porcu et al., 2011).

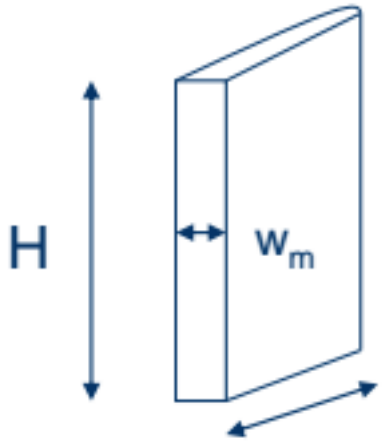

Figure 2.13. KGD-geometry. The fracture height is the same over the whole fracture length, and the width of the fracture at the wellbore is the same for the whole height (Bauer, 2016).

2.2 Introduction to numerical modelling of rock behavior and MDEM in particular

Reservoir monitoring is becoming an increasingly more important tool for hydrocarbon field management and is crucial to optimize future production strategies. Based on information about how the reservoir behaves and fractures propagate, things like well placement and injection/production rate and length can be determined. In an attempt to better understand the mechanisms in the reservoir, numerical models are developed. Continuum models, like Finite Element Methods (FEM) and Finite Difference Methods (FDM), have till now been the dominant methods. A weakness of these models is the inability to treat discontinuities in a dynamic manner (Alassi, 2008). To study discontinuities like fractures and faults, the inherently discontinuous Discrete Element Method (DEM) is an obvious choice. Regardless of any advantages and weaknesses, all the methods are simplifications compared to the reality (Rongved, 2015). In all models, assumptions and approximations are necessary. To model a real rock and its behavior, the rock must be discretized into small elements where the properties of each element can be changed individually. Together, the elements create a mesh that represents the whole formation.

To improve the understanding of how untouched rock mass reacts to stimulation, SINTEF Petroleum Research has developed a simulator called Modified Discrete Element Method (MDEM). A two-dimensional (2D) version is used for the simulations done during this master's thesis. A three-dimensional (3D) version also exists, but it is still under development. To calculate the pore pressure field needed to determine the effective stresses in the fracture code, the 2D fracturing code is coupled with the reservoir simulator, TOUGH2. The fracturing code calculates displacements. The so called permeability model uses the displacements to update permeability and porosity, before the hydraulic parameters are passed to TOUGH2 for new pressure calculations (Lavrov et al., 2016). The workflow is schematically illustrated in Figure 2.14.

Like the name implies, MDEM is a modification of the discrete element method. Compared to continuum approaches like FEM, DEM is a less complicated numerical technique that still can model fracture initiation and propagation with ease. The main advantages of using DEM instead of continuum approaches are (Alassi et al., 2011):

- DEM uses rather simple mathematics, which makes it easier to understand and code.
- DEM naturally deals with discontinuities like fractures and faults and can therefore easily model fracture initiation and propagation.
- DEM uses a dynamic solving scheme, resulting in spontaneously fracture propagation.

DEM has previously been used to model hydraulic fracture processes, but calibration of rock properties has shown to be hard. Instead of Young's Modulus and Poisson's ratio, DEM uses internal stiffness parameters defined at the contacts between the elements (Alassi et al., 2011). To overcome the calibration problems, Alassi (2008) proposed a modification, that led to the development of MDEM. In the new approach, MDEM behaves similar to FEM initially. Only after rock failure it starts to behave like DEM. This way some of FEM's benefits are maintained, and fracture propagation can be handled with ease (Rongved, 2015).

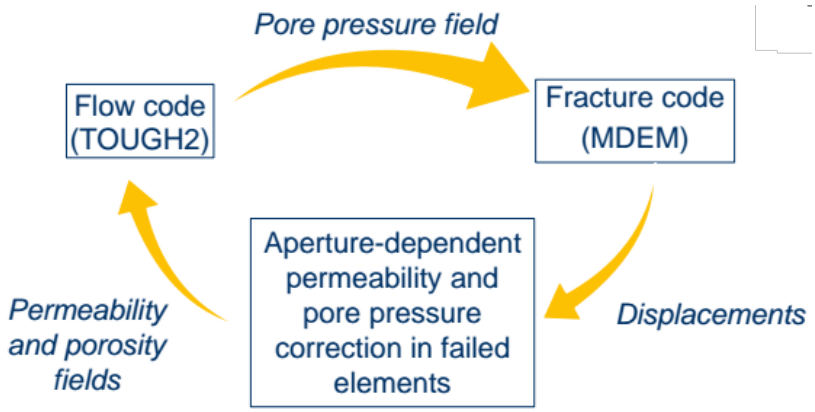

Figure 2.14. Computation flow in a coupled numerical simulation of hydraulic fracturing (Lavrov et al., 2016).

2.2.1 Rock behavior calculations

In the 2D version, MDEM uses a triangular mesh to discretize the modelled rock into hexagonal Voronoi's elements. Each node on the triangles represents the center of an element. As one can see in Figure 2.15, each triangle represents a cluster of three hexagonal elements and contains three contact surfaces. The three normal contact forces, f_n, are calculated by the following model (Alassi et al., 2011; Alassi, 2008: 78):

$$\begin{bmatrix} F_{n1} \\ F_{n2} \\ F_{n3} \end{bmatrix} = \begin{bmatrix} k_{n1} & a_{12} & a_{13} \\ a_{21} & k_{n2} & a_{23} \\ a_{31} & a_{32} & k_{n3} \end{bmatrix} \begin{bmatrix} U_{n1} \\ U_{n2} \\ U_{n3} \end{bmatrix}, \quad \text{Eq. 2.27}$$

where k_{ni} is the normal stiffness of the contacts i = 1, 2, 3, and U_{ni} are the corresponding normal relative displacements. a_{ij} is a newly-introduced stiffness which represents the modification of the original DEM. In a compacted form, it is written

$$F = KU, \quad \text{Eq. 2.28}$$

where K then can be called an internal stiffness matrix. K can be obtained from the conventional constitutive matrix, C. C describes the elastic properties of the material and relates the strain, $\varepsilon = [\varepsilon_{xx}, \varepsilon_{yy}, \varepsilon_{xy}]$, and stress, $\sigma = [\sigma_{xx}, \sigma_{yy}, \sigma_{xy}]$, as

$$\sigma = C\varepsilon. \quad \text{Eq. 2.29}$$

If the cluster's unit normal vector matrix, M, is defines as

$$M = \begin{bmatrix} I_{11}^2 d_1 & I_{12}^2 d_1 & I_{11} I_{12} d_1 \\ I_{21}^2 d_2 & I_{22}^2 d_2 & I_{21} I_{22} d_2 \\ I_{31}^2 d_3 & I_{32}^2 d_3 & I_{31} I_{32} d_3 \end{bmatrix} \quad \text{Eq. 2.30}$$

where $I_{m1} = cos\theta_m$ and $I_{m2} = sin\theta_m$, and the angle θ_m represents the normal vector orientation of the contact m inside the cluster, the following then holds (Rongved, 2015; Alassi, 2008: 79):

$$\sigma = \frac{1}{A} M^T F \quad \text{Eq. 2.31}$$

$$U = M\varepsilon \quad \text{Eq. 2.32}$$

Here, A is the area of a cluster (triangle).

The behavior of the modelled rock is based on the predetermined boundary conditions and interaction between elements. In the 2D version, there is no stress or strain in the out-of-plane direction. 3D reservoir properties are taken as inputs, but they are converted to equivalent 2D values for use in the model (Rongved, 2015: 20-25).

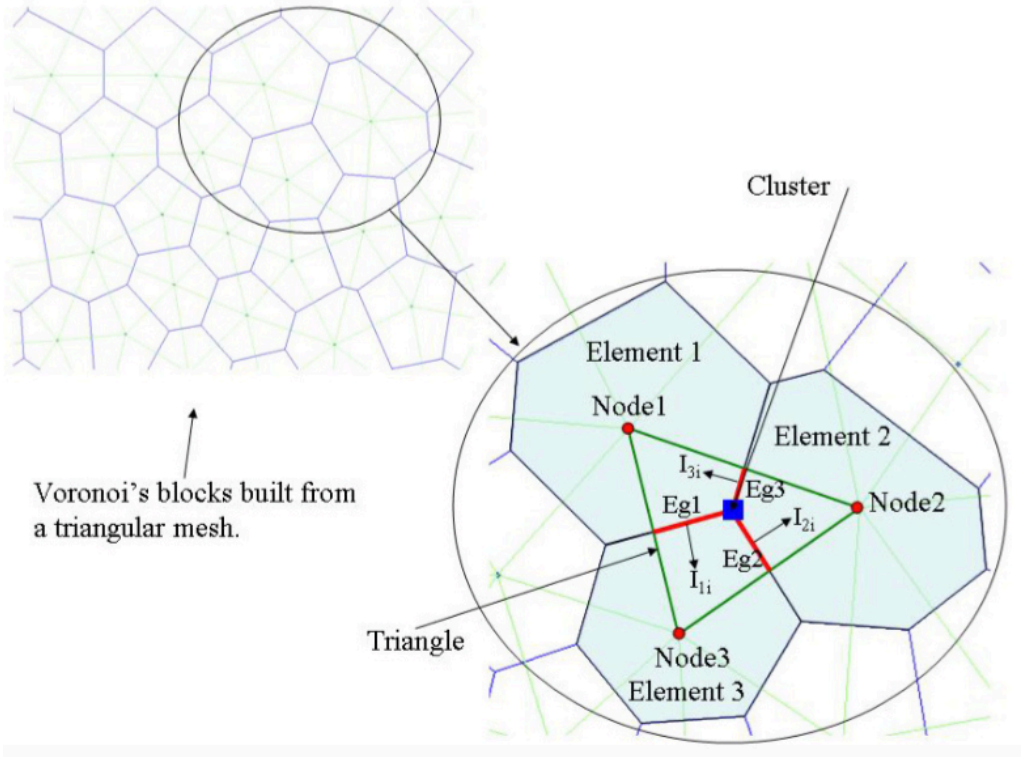

Figure 2.15. The rock mass is represented by Voronoi's blocks built from a triangular mesh. Each triangle represents a cluster of three elements (Alassi, 2008: 81).

2.2.2 Fluid flow model

For fluids to flow, the rock model must contain permeable paths the fluid can follow. The fluid flow model used in MDEM is based on the Finite Difference Method where the spatial discretization is achieved be a network of pipes (Alassi, 2008: 96-97). Figure 2.16 gives a graphical representation of how the pipes match the contacts of the discrete elements and how the domains of the network are made to match the cluster. The flow rates, q_i, in each of the three pipes are given by Darcy's law (Alassi, 2008: 97),

$$q_i = \frac{k_i}{L_i \mu}(P - P_i). \qquad \text{Eq. 2.33}$$

Here, k_i is the permeability of the pipe, L_i is the pipe length, μ is the fluid viscosity, and P and P_i are the pressures of the domain of concern and the other connected domains, respectively. The permeability is calculated for each cluster individually. Since each pipe shares two clusters (see Figure 2.16), the total permeability of a pipe is based on contributions from two sub-pipes connected in series (Alassi, 2008: 98).

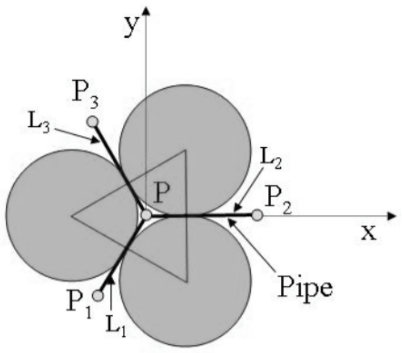

Figure 2.16. The pipe network matches the contacts inside a discrete element cluster (Alassi, 2008: 96).

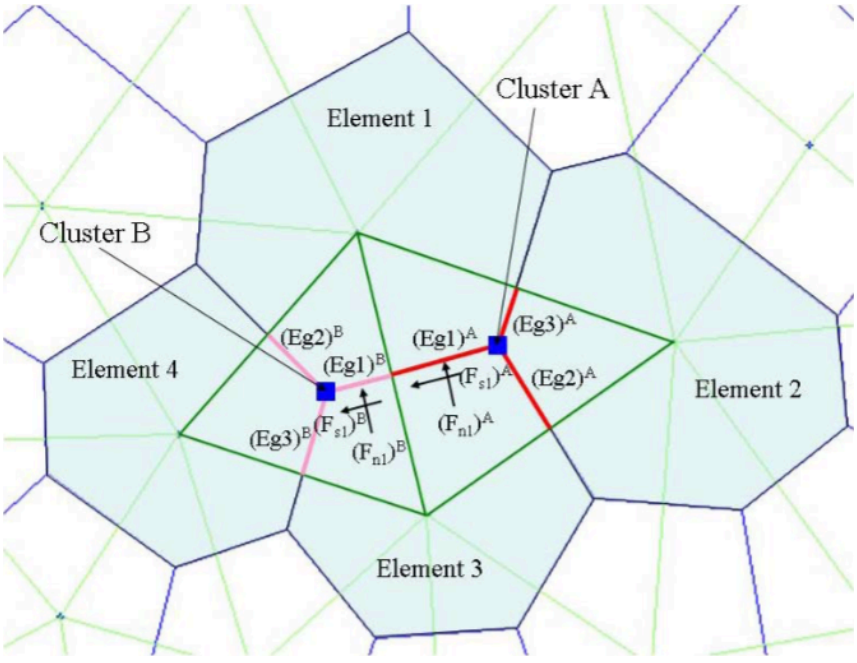

Figure 2.17. The contacts and the pipe networks between two elements share two clusters. Each cluster has its own sub-edge e.g. $(Eg1)^A$ for cluster A and $(Eg1)^B$ for cluster B (Alassi, 2008: 83).

2.2.3 The permeability model

MDEM consists of three main parts. In addition to the MDEM model, that is responsible for the rock behavior calculations, and the flow model, that is responsible for the fluid flow and pressure distribution calculations, a permeability model exists to calculate the permeabilities. The main contributor to fracture permeability is the hydraulic aperture of the fracture. The upscaled permeability of a failed element, k_f, is a function of hydraulic aperture, w, like

$$k_f = {w^2}/{12}. \quad \text{Eq. 2.34}$$

Hydraulic aperture

Hydraulic aperture is defined as the aperture of a smooth-walled fracture conduit that produces the same flow rate under the same applied pressure gradient as a rough-walled fracture. In MDEM, it is the hydraulic, not geometrical, aperture that enters the expressions for fracture permeability (Lavrov et al., 2016).

The hydraulic aperture of a fracture is, in general, a function of (i) the fluid rheology, (ii) the fracture roughness, and (iii) the normal and shear displacement between the fracture faces (Lavrov et al., 2016). The effect of fluid rheology is not considered in MDEM since water is currently the only fluid available. The roughness of fractures affects the hydraulic aperture because the asperities introduce tortuosity to the fluid flow and reduce the flow rate. The effect of fracture roughness is included implicitly through fitting parameters of the model. In Section 2.1.3, three contributions were said to affect the mechanical aperture of a fracture. In MDEM, it is assumed that the hydraulic aperture can be decomposed similarly:

$$w = w_0 + \Delta w_{(n)} + \Delta w_{(s)}. \quad \text{Eq. 2.35}$$

Here, w is the hydraulic aperture of the fracture, w_0 is the initial hydraulic aperture, $\Delta w_{(n)}$ is the change in the hydraulic aperture caused by normal displacement, and $\Delta w_{(s)}$ is the change in hydraulic aperture caused by dilation due to shear displacement.

$\Delta w_{(n)}$ and $\Delta w_{(s)}$ are calculated from normal and shear displacement discontinuities in a failed element. The contribution to hydraulic aperture from normal displacement is simply set to be the normal displacement discontinuity, u_n, times a dimensionless factor, λ (Lavrov et al., 2016):

$$\Delta w_{(n)} = \lambda u_n. \qquad \text{Eq. 2.36}$$

The reduction in hydraulic aperture due to roughness is already discussed. λ, will therefore always lie between 0 and 1. In reality, the relation between hydraulic and geometric aperture is not linear. Smaller geometric aperture causes increasingly more tortuosity to the flow, resulting in an increasingly faster drop in hydraulic aperture (Lavrov et al., 2016). The linear relation used in MDEM (Eq. 2.36) is inaccurate at small u_n, but it is good enough to simulate the most basic behavior.

Shear-dilation

The relation between shear displacement and hydraulic aperture seen from experiments (Figure 2.2) is best described by an exponential function. In MDEM, the shear-induced aperture variation is linked directly to u_n and u_s through this simple model (Lavrov et al., 2016):

$$\Delta w_{(s)} = \begin{cases} (\alpha\sigma - u_n)\left(1 - e^{-\frac{|u_s|}{u_*}}\right) & if\ \alpha\sigma \geq u_n \\ 0 & if\ \alpha\sigma < u_n \end{cases} \qquad \text{Eq. 2.37}$$

Here, σ is the standard deviation of the fracture aperture distribution, u_* is a scaling parameter that determines how fast the aperture increases relative to shear movement, and α is a dimensionless tuning parameter. The tuning parameter, α, should be greater than 1 because the occurrence of shear-dilation depends on the highest asperities, and they will always be greater than the asperities' standard deviation, σ. As see from Eq. 2.37, the shear displacement contribution is dependent on, inter alia, normal displacement and the height of the greatest asperities. A reduced u_n brings the fracture walls closer together and causes asperities to bump into each other more often, thus increasing shear-dilation. From Eq. 2.37, one can see that the value of $\Delta w_{(s)}$ as $u_s \to \infty$ is given by

$$\Delta w_{(s)max} = \alpha\sigma - |u_n|. \qquad \text{Eq. 2.38}$$

The equation states that the effect of shear-dilation on hydraulic aperture becomes less pronounced as u_n increases until the asperities no longer touches and $\Delta w_{(s),max} = 0$. In Figure 2.1c, it has come to this point, and thus, no further shear-dilation will occur. This is accounted for in the inequalities in Eq. 2.37.

3 Problem Description and Numerical Scheme

The presence of natural fractures and the roughness of fracture walls have shown to affect the results of hydraulic fracture treatments, both individually and combined. Individually, natural fractures affect the fracture pattern, while shear-dilation is known to increase the hydraulic aperture of fractures. Combined, the two increase the stimulated volume. To evaluate the final result of a fracture treatment, a fall-off test is a cheap and easy method that can give lots of information. The goal of this thesis is to compare MDEM results with field experiences and physical explanations and, through that, get a better understanding of fracture mechanics. All simulations in this thesis are done under fracture treatment operations where hydraulic fractures are created. The focus will be on exploring the effects of

- a natural fracture intersecting the borehole,
- fracture and formation properties on fall-off curves,
- shear-dilation in rough-walled fractures, and
- altered viscosity of the injection fluid.

3.1 Physical description

Horizontal wells with induced hydraulic fractures are widely used to maximize the contact between the formation and the well. In the following simulations, it is assumed that a horizontal well is drilled in the direction of the intermediate principal stress, perpendicular to the minimum and maximum principal stresses. The borehole has a diameter of 0.3 meters, and it is open to the formation and natural fractures. All the simulations have been done with the same isotropic stress field, where $\sigma_v = 30$ MPa and $\sigma_H = 35$ MPa, and the same initial pore pressure of 20 MPa. A vertical well with intermediate principal stress in the vertical direction would have given the same results.

PhD candidate at The Department of Petroleum Engineering and Applied Geophysics, Mats Rongved, has earlier run simulations with a natural fracture intersecting the borehole in impermeable formations. For the simulations done in this thesis, a highly porous and permeable formation is used. For numerical simplicity, the formation is assumed homogeneous and intact. The same rock properties were used in all simulations, and they are summarized in Table 3.1.

Table 3.1. Summary of rock properties used in the MDEM simulations.

Property	Value
Elastic modulus (GPa)	15
Poisson's ratio	0.25
Tensile strength (MPa)	4
Shear strength (MPa)	15
Matrix density (kg/m^3)	2700
Porosity (%)	50
Permeability (m^2)	5e^{-15}

3.2 Numerical description

The simulations presented in this thesis are done in the 2D version of MDEM, and so, the rock matrix is represented by a two-dimensional mesh. The mesh is 100x100 meters and consists of 30630 different elements. An illustration of the mesh can be seen in Figure 3.1. To give the 2D grid a volume, the depth of each element is set to be 10 meters. As shown in Figure 3.1, the node density increases towards the middle of the mesh, with a 1x10 meters area of extra small elements in the center. In the center region, the area of each triangle is about 4 cm^2. To obtain good results, the fracturing should happen well within the area of extra high node density.

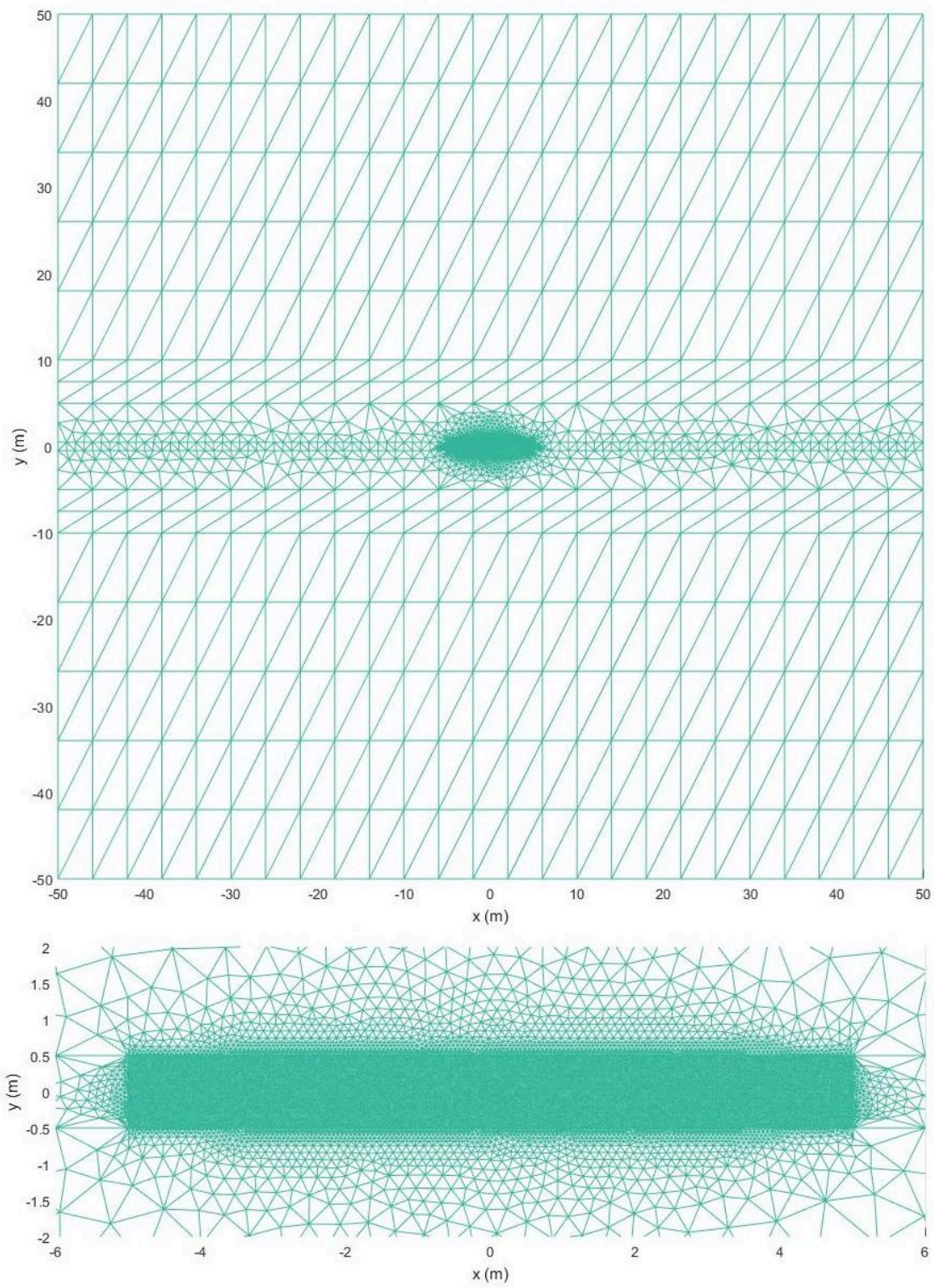

Figure 3.1. Illustrations of the whole mesh (top) and an enlargement of the center of the mesh (bottom).

3.3 Problem descriptions

Natural fractures intersecting the borehole & the resulting fall-off curves

Two different cases are simulated to look at the effects of a natural fracture intersecting the borehole; one where the natural fracture is in the direction of the maximum principal stress (case 1), and one where the natural fracture is tilted 45° relative to the maximum principal stress (case 2). The two cases are presented in Figure 3.2. In both cases, the length of the natural fracture is 1.1 meter from tip to tip. To see how injection rate affects the fracture propagation, each case is run with three different injection rates, making it six different simulations in total. An overview of each simulation is presented in Table 3.2.

After a given time, the well is shut in to do a fall-off test and create fall-off curves. To get proper comparisons, the simulations with equal injection rate, but different angles on the natural fracture, are shut in at the approximately same time. For best comparisons between the simulations with different rates, several ways of deciding the time of shut-in was discussed; the wells could be shut in after the same amount of time, the same amount of injected mass, or after the fracture propagation had stabilized. The initial plan was to wait for the fractures to stabilize, but because of limited time, the time of shut-in ended up being pretty random. The shut-in times are presented in the last column of Table 3.2. To validate the accuracy of the fall-off curves and see if the estimations coincide with the actual results, the approach described by Marongiu-Porcu et al. (2011) are used on a pressure profile obtained from MDEM. Using MDEM to analysis fall-off curves and better understand the fractures is an application the industry has sought and asked about.

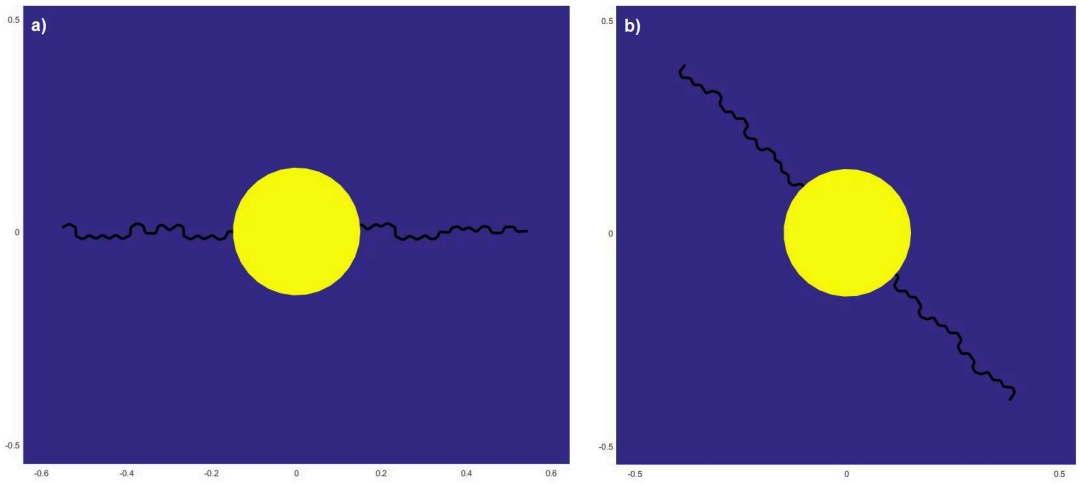

Figure 3.2. Illustrations of the a) 0° and b) 45° predefined fractures. The yellow areas are the cross-sections of the wells. The black lines are the natural fractures.

Table 3.2. Overview of the varying parameters used in simulation done to look at fracture intersection and fall-off curves. q is the injection rate, θ is the angle of the natural fracture relative to the maximum principal stress, and t_e is the length of injection before shut-in.

Simulation no.	q (kg/s)	θ (°)	t_e (s)
1	1.6	0	8596
2	1.6	45	8601
3	1.8	0	5194
4	1.8	45	5205
5	2.2	0	1665
6	2.2	45	1661

Shear-dilation in rough-walled fractures

The complexity of fracturing fluids needed to optimize proppant placement was briefly mentioned in Section 2.1.5. In MDEM, only water is injected. There is no way to add solids, and there is no way to change the fluid rheology. Because of the limited injection options, the final results of a conventional fracture treatment simulation will be inaccurate. After the treatment, the fractures close, and no extra permeability will be seen. To avoid this issue, the idea is to mimic the behavior experienced with water-fracs and use the effect of shear-dilation to keep the fractures open also after the treatment is ended. For the idea to work, the shear displacement usually seen during injection must persist also after the well is shut in, and by that

maintain some fracture aperture. If the final effect of shear-dilation is the same as of proppants, tuning the shear-dilation parameters can be done as an alternative to simulate actual injection of proppants.

In previous MDEM simulations $\Delta w_{(s)}$ has been set to zero, and shear-dilation has been neglected. To test the potential of the shear-dilation feature, the feature has been applied in two different fracture treatment simulations. The first simulation was done with MDEM's standard shear-dilation parameters found in the "InProp.m"-file. In the second simulation, the simulated asperity heights were doubled through a doubling of the $\alpha\sigma$-term. The shear-dilation parameters used are presented in Table 3.3. As seen from Eq. 2.37, shear-dilation is dependent on shear displacement, u_s. For the parameters used in the two simulations, the effects of shear-dilation relative to shear displacement are calculated and presented in Figure 3.3. From the graphs, it can clearly be seen how the shear-dilation increases with increasing shear displacement. The simulations are done with a tilted natural fracture (case b in Figure 3.2) to maximize the shear displacement in the fractures. A simulation where the shear-dilation feature is turned off is used as a base case (simulation number 7).

Table 3.3. Overview of the varying parameters used in simulations done to look at shear-dilation. q is the injection rate, θ is the angle of the natural fracture relative to the maximum principal stress, and t_e is the length of injection time before shut-in.

Simulation no.	q (kg/s)	θ (°)	u_* (m)	σ (m)	α	t_e (s)
7	1.8	45	$1e^{-3}$	0	0	2345
8	1.8	45	$1e^{-3}$	$5e^{-4}$	1.5	2335
9	1.8	45	$1e^{-3}$	$10e^{-4}$	1.5	2330

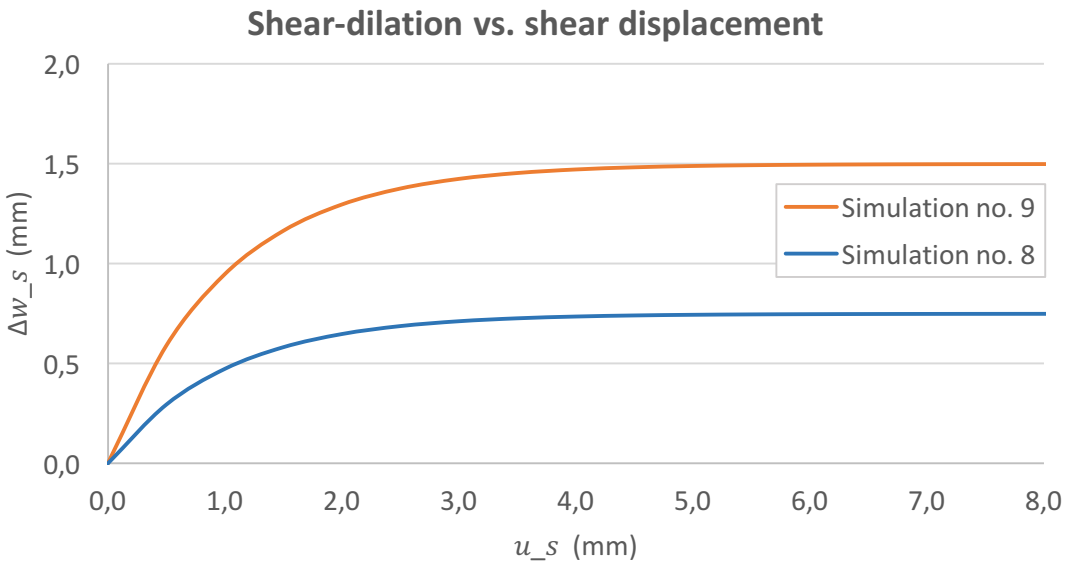

Figure 3.3. The maximum effect of shear-dilation relative to shear displacement for simulation number 8 and 9. The calculations are based on Eq. 2.37.

Fluid rheology

So far, only water has been used in MDEM simulations. Water is a Newtonian fluid with a viscosity of 1 cP. This value is predefined in MDEM and is currently not possible to change without rewriting the code. Drilling and fracking fluids are generally much more complex than so, typically pseudoplastic and thixotropic. A simulator only able to run with water will have limited utility for the petroleum industry. The ability to run MDEM with different viscosities and rheological models will greatly expand its areas of use.

Even though no changeable viscosity parameter is implemented in MDEM, there is another parameter that can be changed to give a similar result. The flow model in MDEM is based on Darcy's law where viscosity and permeability are inverse proportional (see Section 2.2.2 and Eq. 2.33). The effect of multiplying the permeability by a factor will, in theory, give the same effect as multiplying the viscosity by the reciprocal. To describe the approach with an example: if both matrix and fracture permeability is halved, it will give the same result as if the viscosity is doubled.

$$q_2 = \frac{k_1}{L(2\mu_1)}\Delta P = \frac{(k_1/2)}{L\mu_1}\Delta P. \qquad \text{Eq. 3.1}$$

In MDEM, the matrix permeability of the formation is a changeable parameter in the main script. To change the permeability of the fractures, a bit more knowledge about the program is needed, but only one extra line of coding is necessary. A so called permeability multiplier based on, inter alia, fracture aperture is constantly being calculated for each failed element. This parameter can easily be multiplied by the same factor as the matrix permeability. The approach was tested on case b in Figure 3.2 with an injection rate of 1.0 kg/s. The low injection rate was chosen because of the reduced leak-off caused by the increased viscosity (or decreased permeability). Simulation number 4, with an injection rate of 1.8 kg/s, is used for comparison. The higher injection rate is required to create fractures within a reasonable period of time. An attempt was done with an injection rate of 1.0 kg/s, but there were no signs of fracturing. The parameters used are presented in Table 3.4. The approach obviously only work for Newtonian fluids where the viscosity stays constant regardless of shear rate and shear rate history. More advanced programming must be done for MDEM to work with non-Newtonian fluids.

Table 3.4. Overview of the different parameters used in simulations done to look at altered viscosity. k_{matrix} is the matrix permeability and PMX is the permeability multiplier used to estimate the permeability of fractures.

Simulation no.	q (kg/s)	θ (°)	k_{matrix}	PMX
4	1.8	45	$5.0e^{-15}$	PMX
10	1.0	45	$2.5e^{-15}$	PMX/2
11	1.0	45	$2.5e^{-15}$	PMX/2

4 Results and Discussions

This chapter consists of the results contained from the different simulations and the following discussion. Not to confuse the reader, the results of each topic are discussed before the results of the next topic are presented.

4.1 Natural fractures intersecting the borehole

4.1.1 Results

The following figures present the fracture propagation from the simulations done on natural fractures intersecting the borehole. The propagation in each simulation is presented through five pictures at five different times. The black line is the predefined fracture, while the green lines are the hydraulically induced fractures. The colorbar represents the effective stress in y-direction. After the figures, a table summarizes some characteristics of the fractures.

Simulation 1

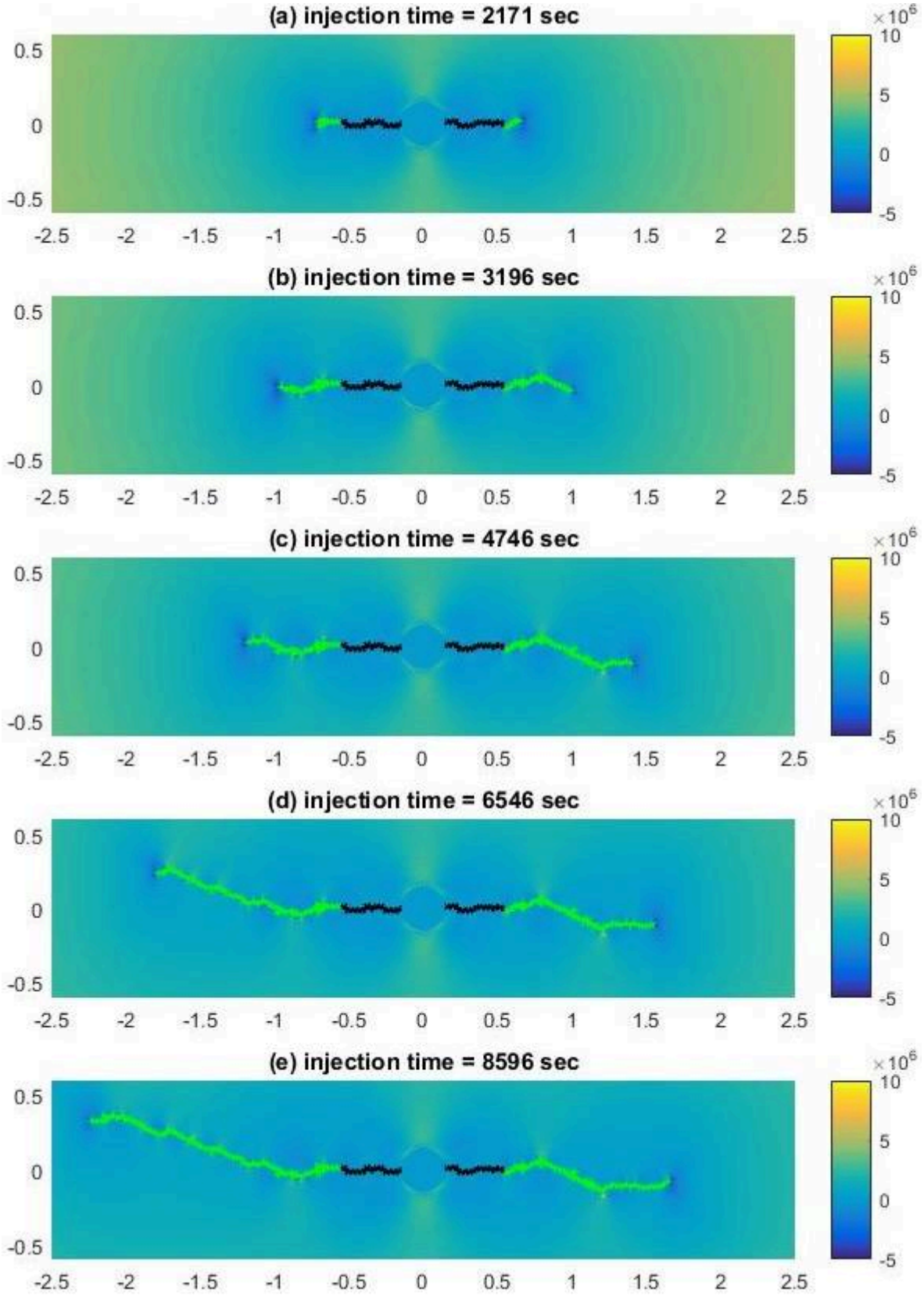

Figure 4.1. The fracture propagation in case 1 with 1.6 kg/s injection rate.

Simulation 2

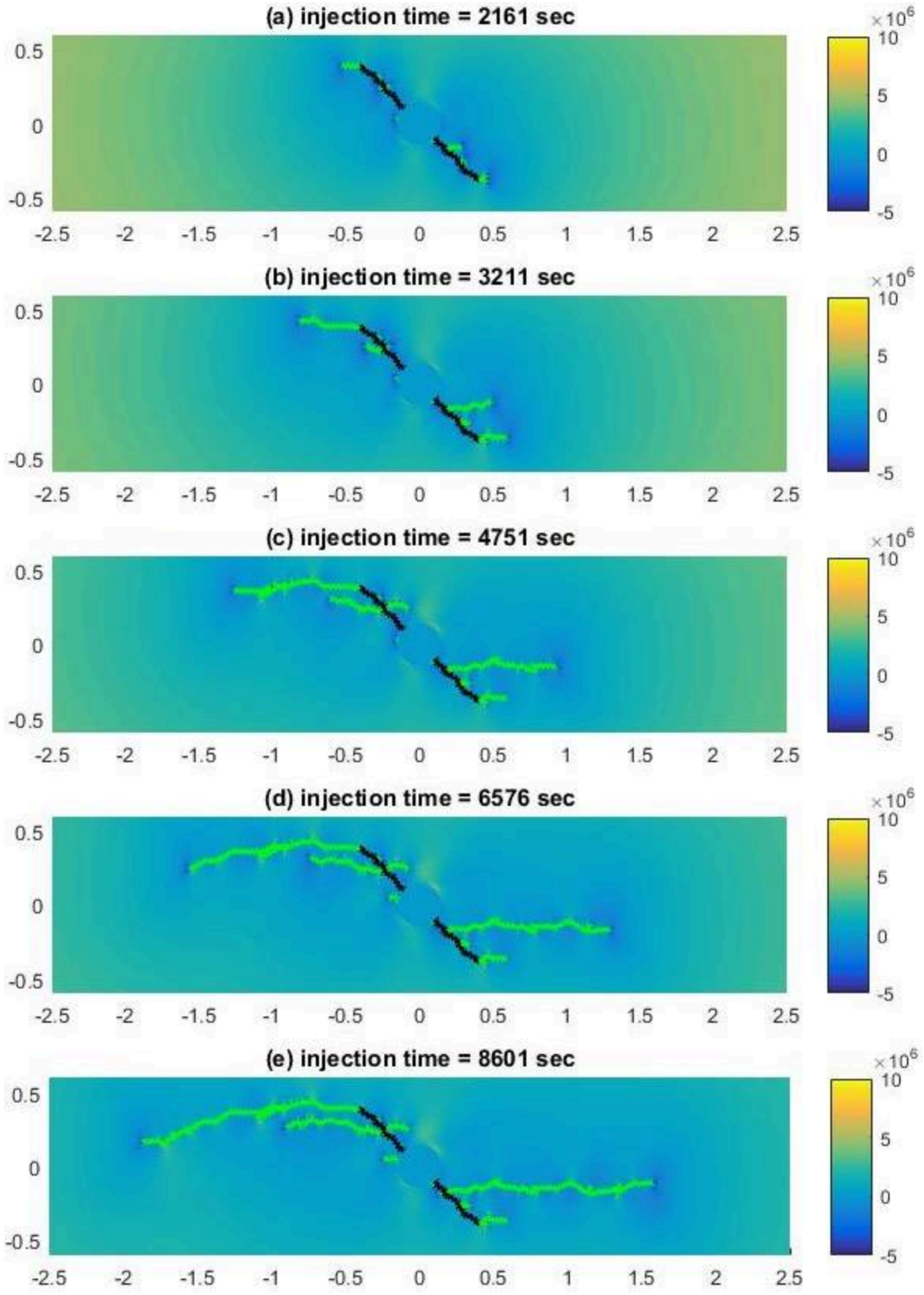

Figure 4.2. The fracture propagation in case 2 with 1.6 kg/s injection rate.

Simulation 3

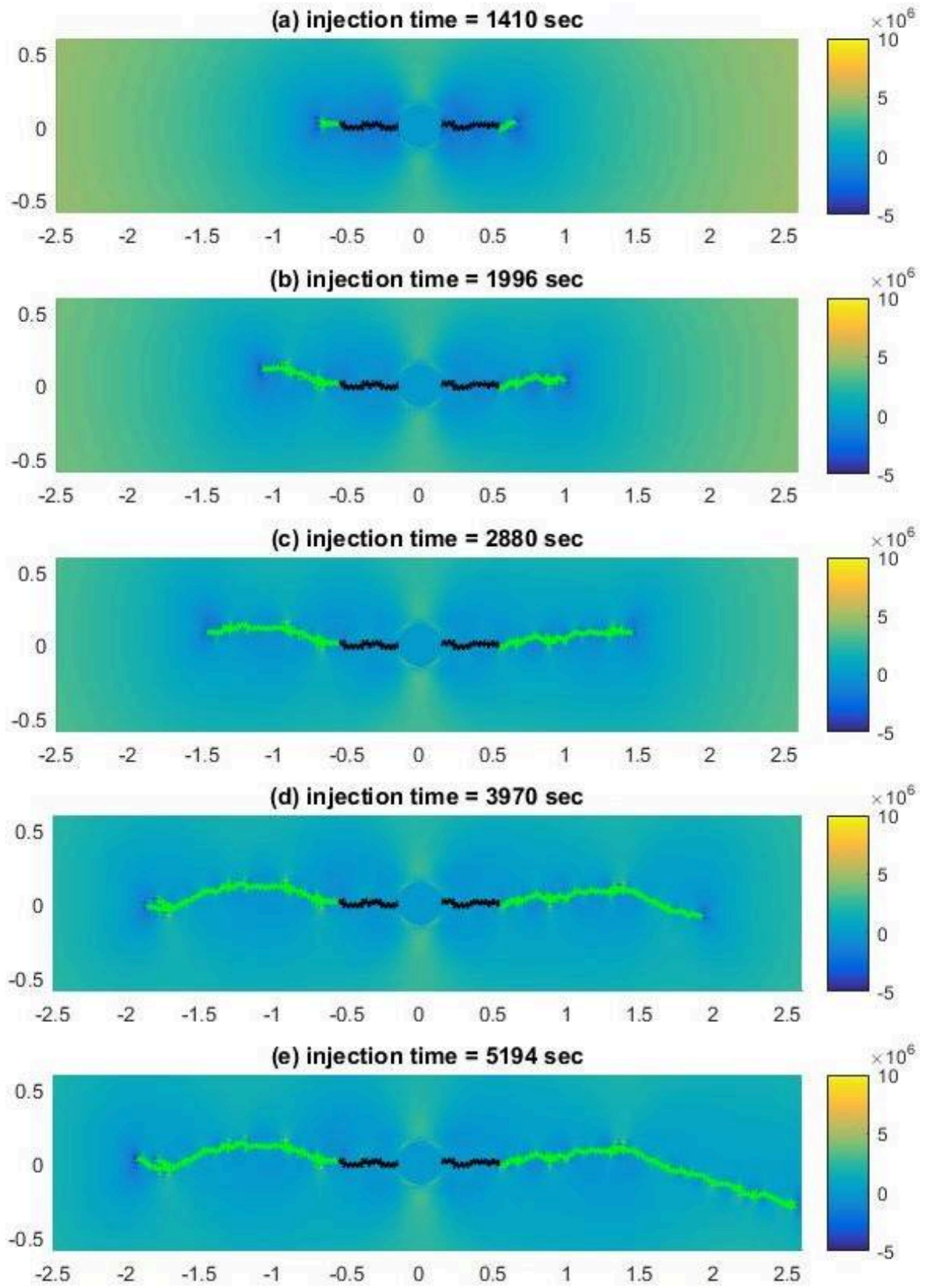

Figure 4.3. The fracture propagation in case 1 with 1.8 kg/s injection rate.

Simulation 4

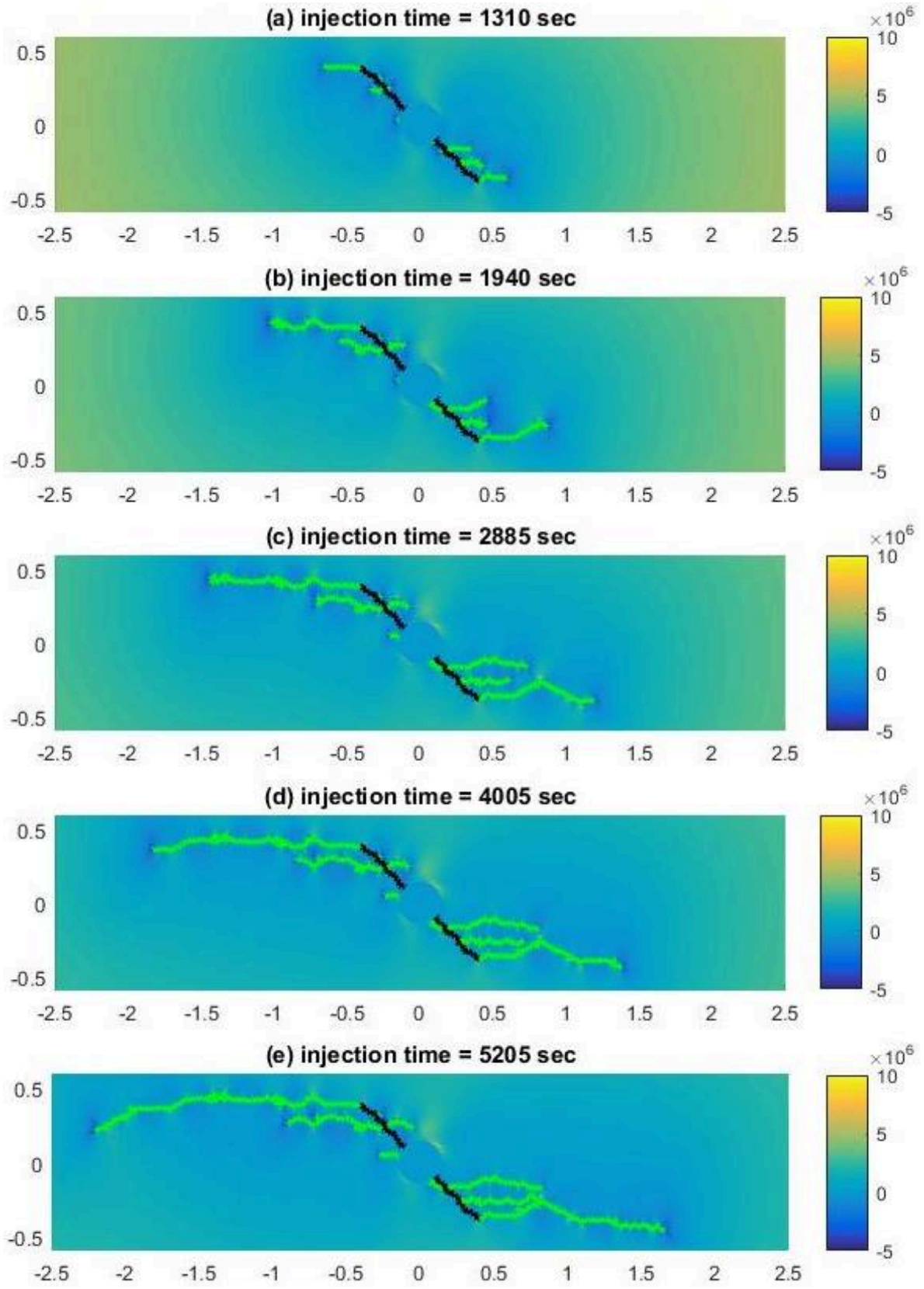

Figure 4.4. The fracture propagation in case 2 with 1.8 kg/s injection rate.

Simulation 5

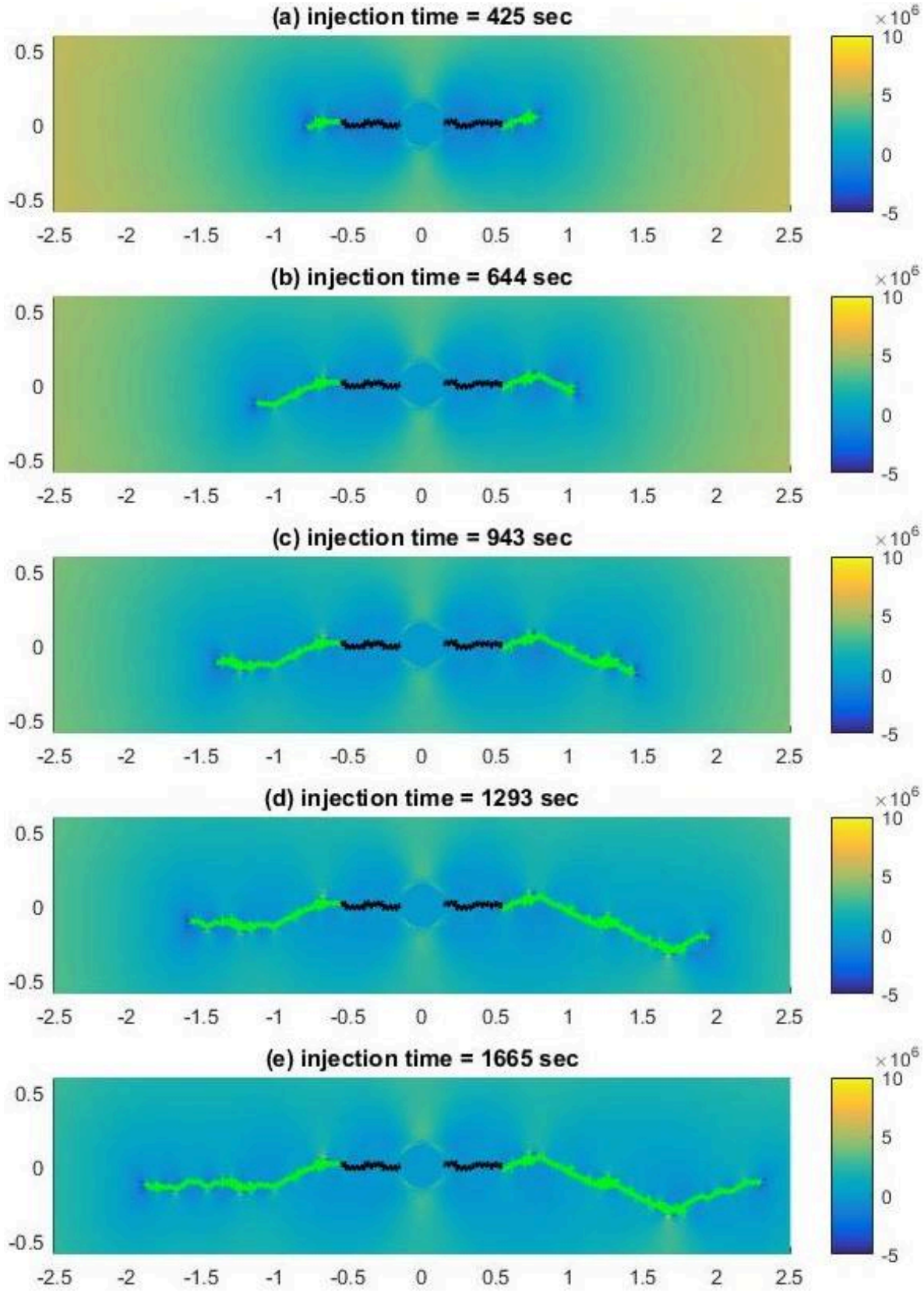

Figure 4.5. The fracture propagation in case 1 with 2.2 kg/s injection rate.

Simulation 6

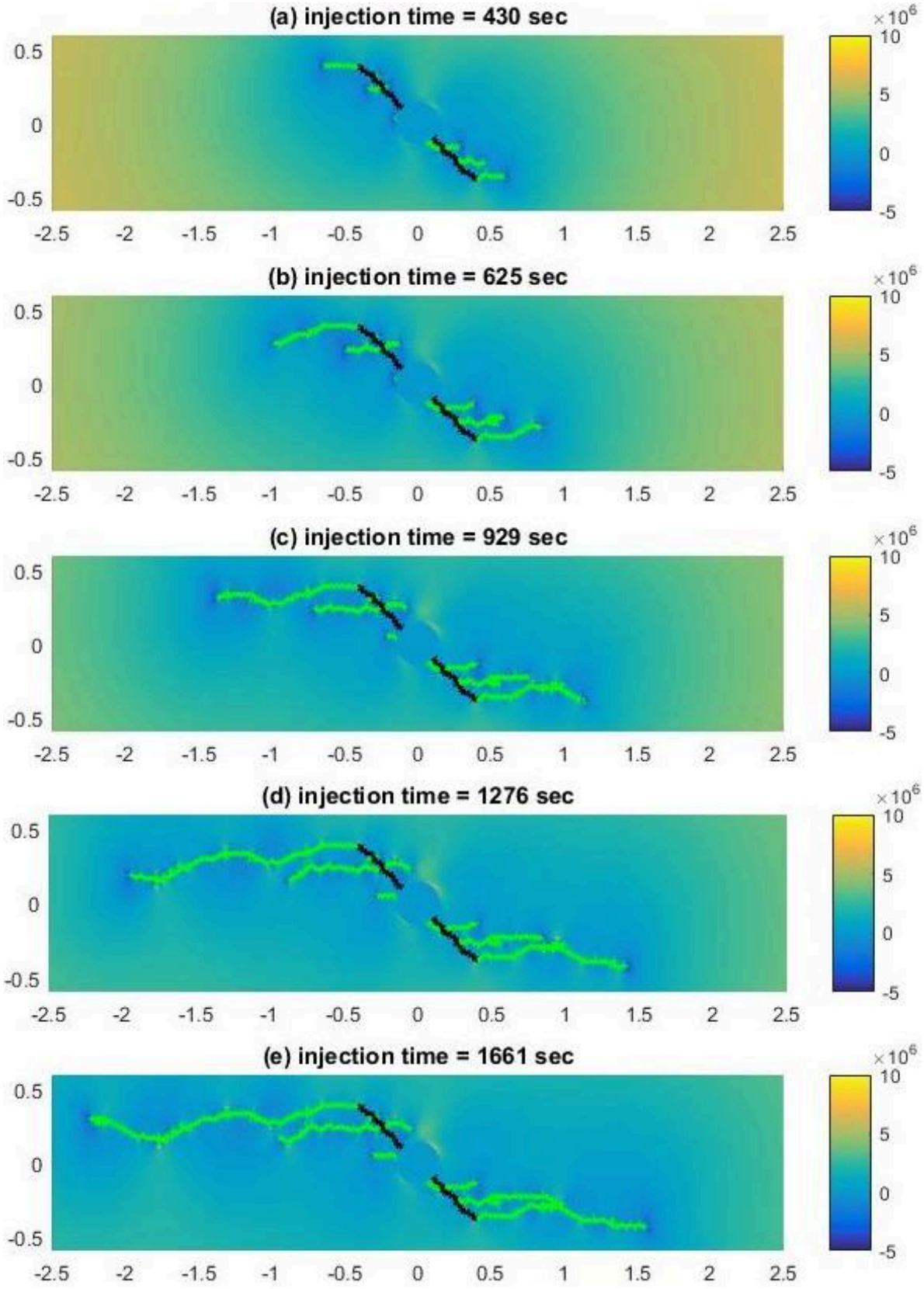

Figure 4.6. The fracture propagation in case 2 with 2.2 kg/s injection rate.

Table 4.1. Fracture characteristics in simulations done with different natural fracture patterns. L_{tot} is the combined length of all fractures, $L_{longest}$ is the longest distance from one fracture tip to the fracture tip on the other side of the borehole in x-direction, included the diameter of the borehole, and TFE is the total number of failed elements.

Simulation no.	**1**	**2**	**3**	**4**	**5**	**6**
L_{tot} **(m)**	4.82	6.05	5.77	7.65	5.66	7.38
$L_{longest}$ **(m)**	3.89	3.43	4.46	3.86	4.18	3.82
TFE	554	736	688	916	660	900

4.1.2 Discussion

To look at the consequences of natural fractures, the cases with equal injection rate and injection period are compared (simulation 1v2, 3v4, and 5v6). Based on the simulations, it is no doubt natural fractures impact the result of fracture treatments. Even though the lengths of all fractures combined in the simulations done with tilted natural fractures are about 1.3 times longer than in the simulations done with flat natural fractures, the fracture half-lengths are shorter. The reason can clearly be seen from the propagation patterns. With a flat natural fracture, all the injected fluid is working on propagating one induced fracture from the tip of the natural fracture. With a tilted natural fracture, several, shorter fractures propagate out from the walls of the natural fracture.

Fractures will always grow in the direction of least resistance, and, generally, that means perpendicular to the minimum principal stress (σ_3). With a natural fracture already in the direction perpendicular to σ_3, it is obvious that an induced fracture will follow the same path. In the case of a tilted natural fracture, it becomes more complex. Instead of two, six main fractures are created in all the three simulations. All fractures are growing in the direction perpendicular to σ_3. However, with the stress shadowing effect in mind (Geilikman et al., 2013), one should expect only one fracture to be induced in each direction. As the fracture aperture expands and pushes away the rock, the stress normal to the fracture increases. Higher pressure is therefore needed to create fractures parallel to each other than if only one fracture is present. In addition, the wedge effect introduced in Section 2.1.1 should favor further propagation in one fracture instead of initiating new ones.

In earlier simulations, like the one presented in Figure 4.7, only one fracture propagated in each direction. However, the permeability used in Figure 4.7 is more than five orders of magnitude less than the permeability used in this thesis. Lower permeability results in less leak-off and lower pore pressure around the fracture. Experiments have shown that pore pressure contributes to the energy available for tensile fracture and that fracture propagation is affected by pore pressure fields (Bruni and Nakagawa, 1991; Cleary, 1979). The increased number of individual fractures seen in the simulations indicate the same influence of pore pressure. With several, parallel fractures, leak-off from one fracture can actually aid propagation in other fractures. In addition, the leak-off is reduced because the fractures work together to charge the surrounding formation. Reduced leak-off might be a reason for the increased total fracture length seen in simulations with a tilted natural fracture compared to simulations with a flat natural fracture.

The induced fractures that propagate out of the tilted natural fracture are initiated at the exact same places in all three simulations. A closer look reveals that these points coincide with irregularities in fracture directions. The results indicate a strong correlation between irregularities and fracture initiation and show the impact irregularities can have on the final result of fracture treatments. The extent of irregularities is not a parameter controlled in MDEM, but a numerical artifact caused by grid effects from the mesh used to represent the formation. Irregularities and heterogeneities are common in reality, and the grid effects are thus not necessarily a drawback. The grid effects can actually be used as a tool to better describe the behavior seen in real fractures.

From the simulations it is found that both the angel of the natural fractures, irregularities in the fracture direction, and the permeability of the matrix influence the final fracture pattern after a fracture treatment. To optimize well placement and treatment processes, all the mentioned factors must be taken into account.

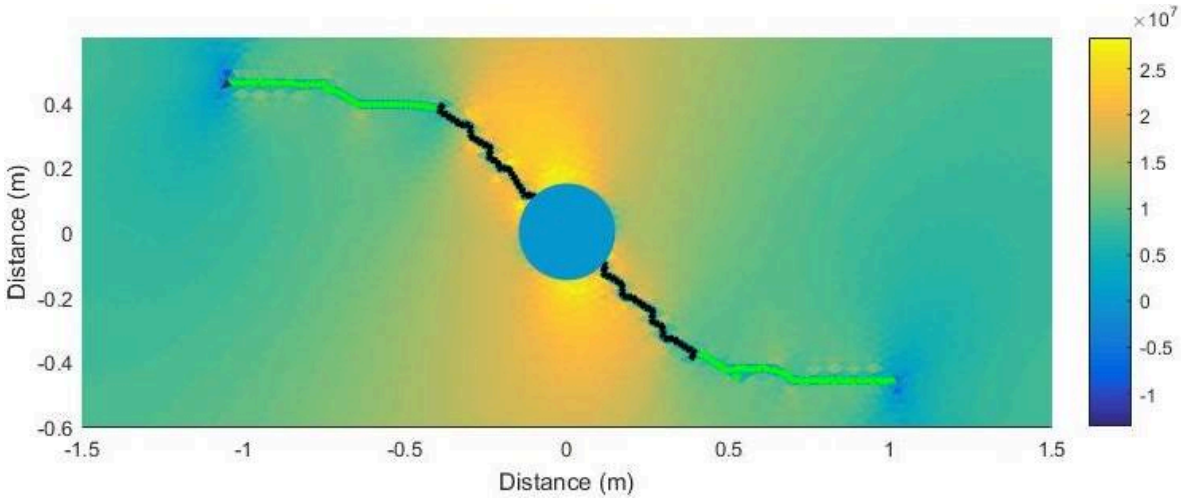

Figure 4.7. The fracture propagation seen in a formation with $2e^{-21}$ m^2 permeability. The simulation is done by Mats Rongved.

4.2 Fall-off test

4.2.1 Results

Leak-off rate strongly affects a fall-off test. To better understand the concept of leak-off, fracture propagation in a growing fracture simulated in MDEM is presented in Figure 4.8. Figure 4.9 is an attempt to estimate fracture closure pressure through a loglog plot. The approach is based on the method explained by Marongiu-Porcu et al. (2011) and presented in Section 2.1.6.

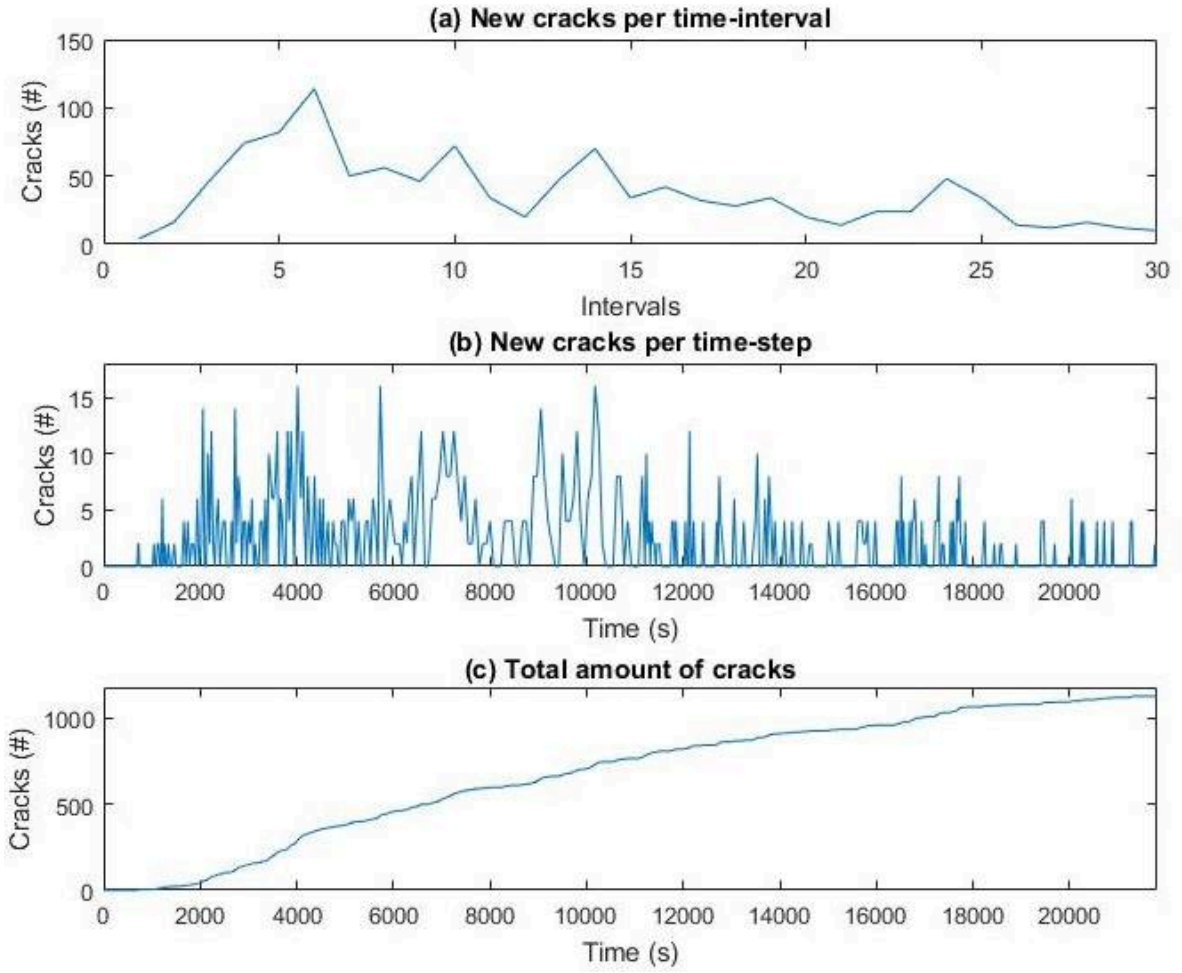

Figure 4.8. Fracture extent's affect on fracturing rate. (b) shows the number of new cracks per time-step, while in (a), the time-steps are gathered in intervals. (c) shows the total amount of failed elements vs. time. The x-axis represents the same time period in all the plots.

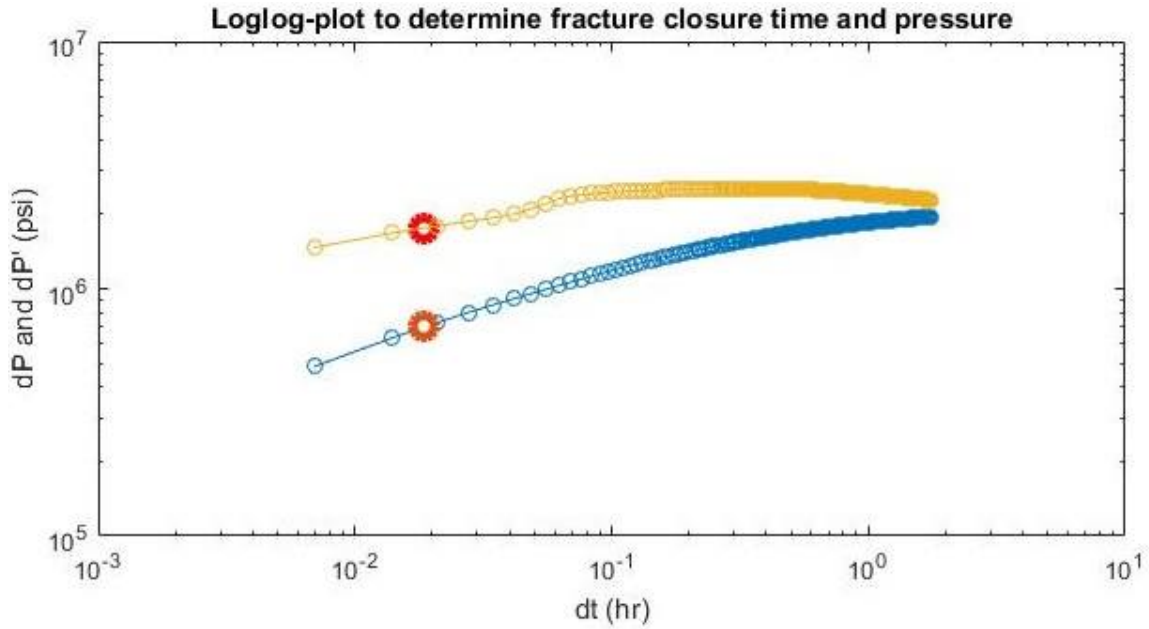

Figure 4.9. Closure pressure determination through loglog plot. The yellow line is $\Delta p'$, and the blue line is Δp. Each circle represents a data point. The large, red circles indicate the time when fracture closure actually happened.

4.2.2 Discussion

A simulation was conducted to better understand the effect of leak-off on propagation rate. Figure 4.8 shows the fracture propagation in a quantitative way. In the initial phase of a fracture treatment, some time is needed for the pressure to build up and exceed the breakdown pressure. The pressure doesn't only increase in the well during this period; Also the surrounding formation will experience increased pressure. After fracture initiation, the well pressure is kept fairly constant around the fracture propagation pressure. As the formation pressure keeps increasing, the leak-off decreases. The fracture propagation rate reaches its maximum (after approximately 4000 seconds in Figure 4.8). After the peak, the rate gradually decreases as larger areas are opened to leak-off. Eventually, the leak-off area is large enough for the formation to absorb almost all the injected fluid, and thus, the fracture stabilizes. Leak-off is the main contributor in fall-off tests, and after the effect fracture extent has on leak-off is seen, it is understandable how fracture length can be estimated through fall-off tests.

Before the equations in Section 2.1.6 can be used for estimation of fracture properties (Eq. 2.23-2.26), the fracture closure time and pressure must be estimated. The fracture closure pressure

(σ_3) is known in MDEM and can therefore easily be compared to the results given by the loglog plot in Figure 4.9. The figure shows the response with pressures obtained from MDEM. It is clearly different from the ideal response presented in Figure 2.12, and the fundamental 3/2 slope is absent.

The actual point of fracture closure was also plotted in Figure 4.9 (red circles). Due to large leak-off, fracture closure occurs shortly after shut-in. The graphs show a limited number of data points before fracture closure (2), and the density of data points around the time of fracture closure is not good (25 seconds between each measurement). Even though the MDEM results didn't match the ideal loglog plot, it is hard to say anything about its appliance before a more representative fall-off test is simulated.

4.3 Fracture roughness

4.3.1 Results

The first figure in this section presents the final fracture patterns in the three simulations with different fracture roughness. Figure 4.11 and Figure 4.12 show the hydraulic apertures at end of injection and after fracture closure, respectively, for the same simulations. The colorbar in Figure 4.12 has a limited maximum value for better resolution of the smaller apertures. All apertures larger than $2*e^{-5}$ thus show up with the same, yellow color. The exact apertures can be seen in the following graphs. Among the graphs, the left columns correspond to the values seen in Figure 4.11, and the right columns correspond to the values seen in Figure 4.12. For better comparison between the simulations, Figure 4.13 is dedicated to the fractures on the upper, left side of the borehole, while Figure 4.14 is dedicated to the fractures on the lower, right side. At the end, the enhanced permeability after fracture closure is shown.

Fracture patterns in formations with different fracture roughness

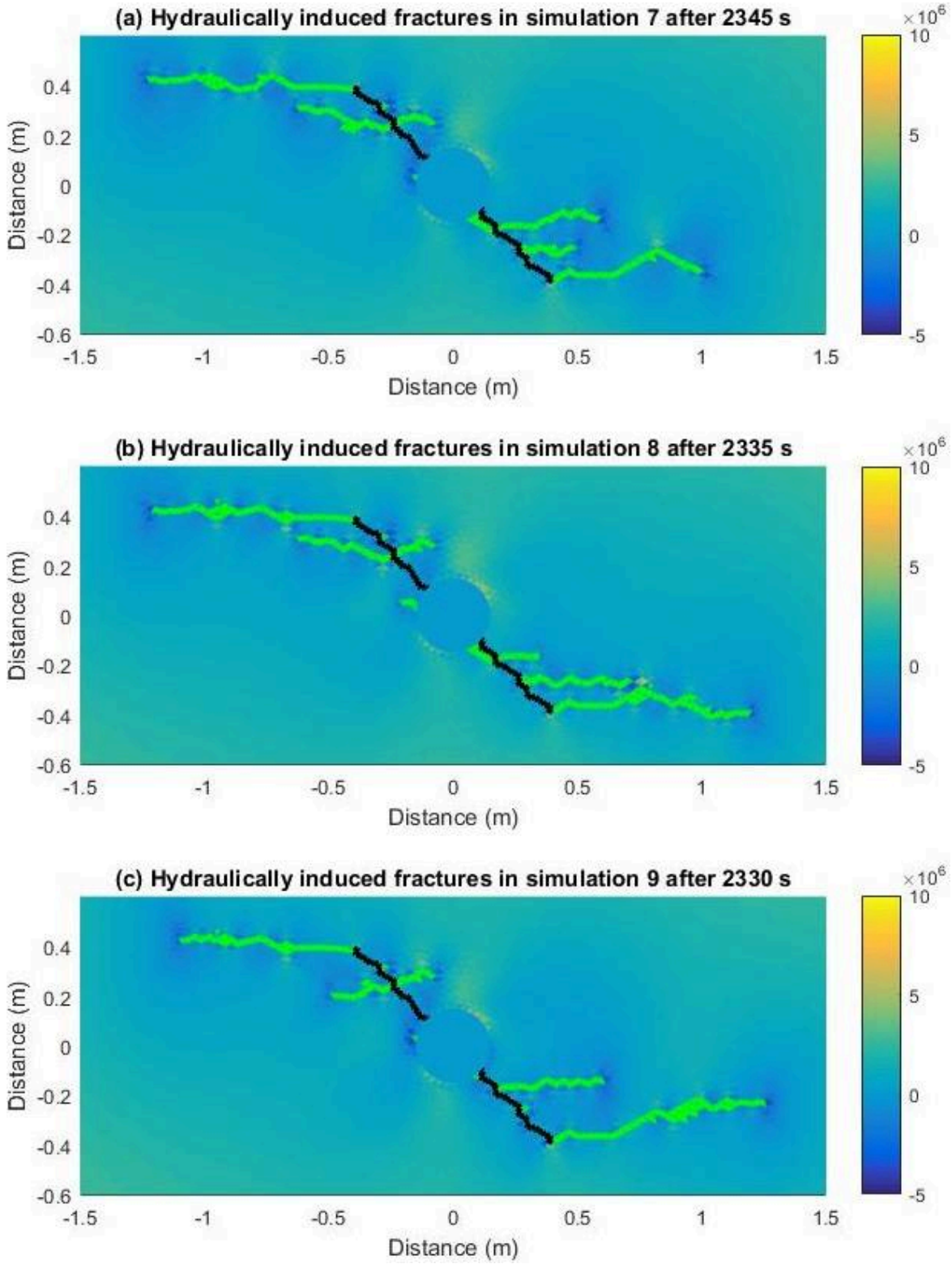

Figure 4.10. Hydraulically induced fractures after fracture treatment. (a) is with smooth fracture walls. The asperities in (b) are 0.75 mm, and the asperities in (c) are 1.5 mm. The colorbar represents the effective stress in y-direction.

Hydraulic apertures at end of injection

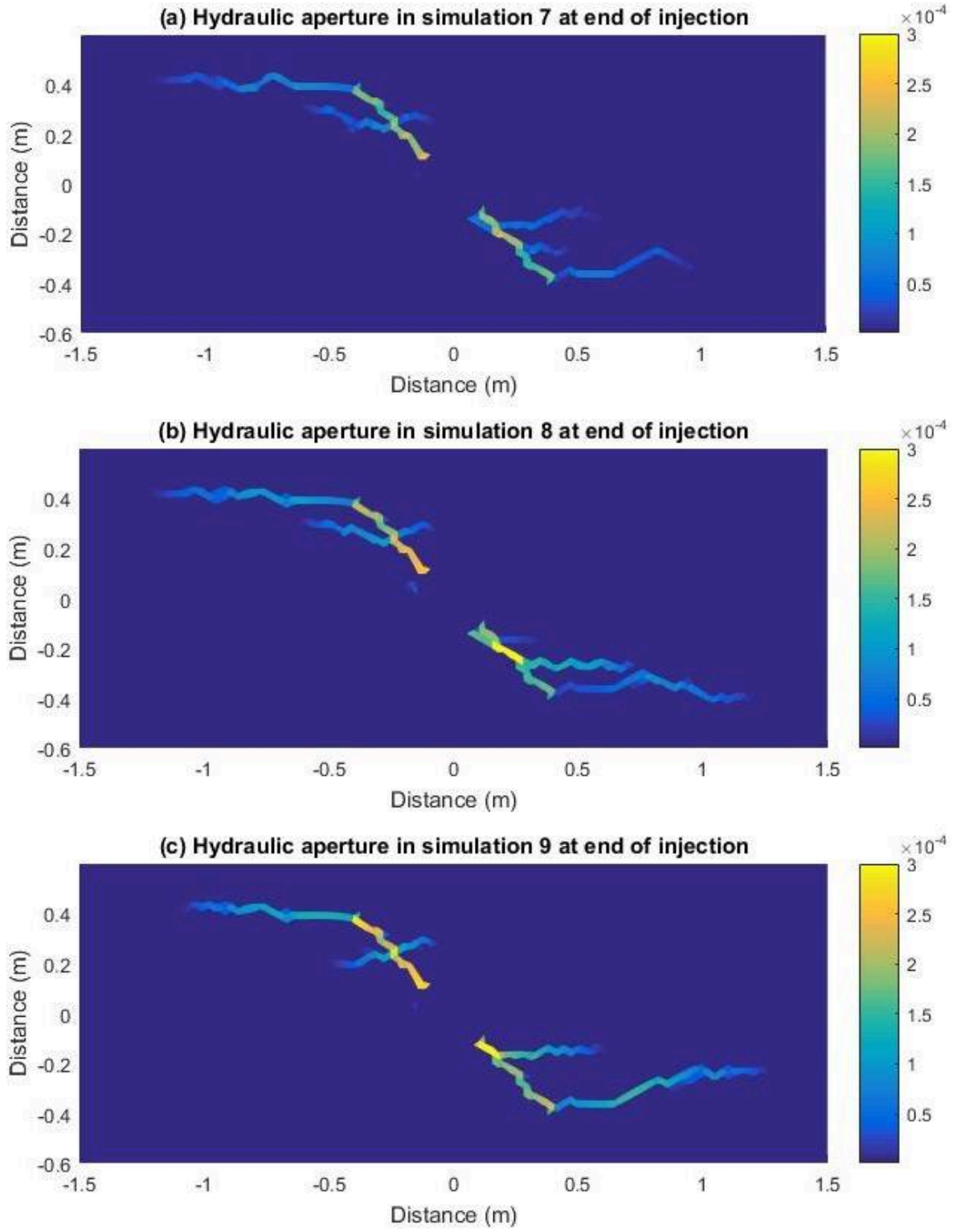

Figure 4.11. The hydraulic apertures in the fractures at end of injection. (a) is with smooth fracture walls. The asperities in (b) are 0.75 mm, and the asperities in (c) are 1.5 mm. The colorbar represents the hydraulic aperture in meters.

Hydraulic apertures after fracture closure

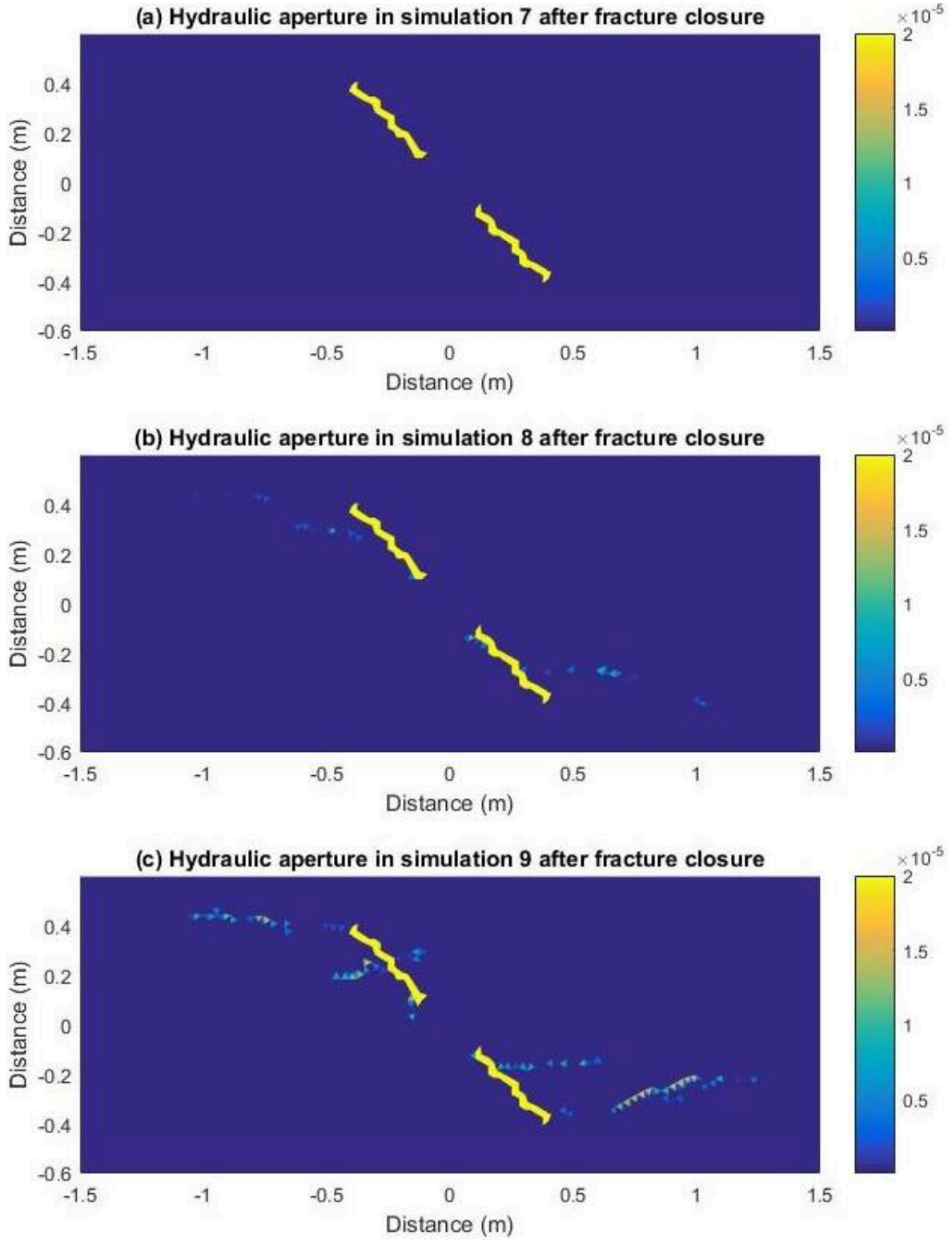

Figure 4.12. The remaining hydraulic aperture in the fractures after fracture closure. (a) is with smooth fracture walls. The asperities in (b) are 0.75 mm, and the asperities in (c) are 1.5 mm. The colorbar represents the hydraulic aperture in meters.

Hydraulic aperture of the fractures on the upper, left side of the borehole

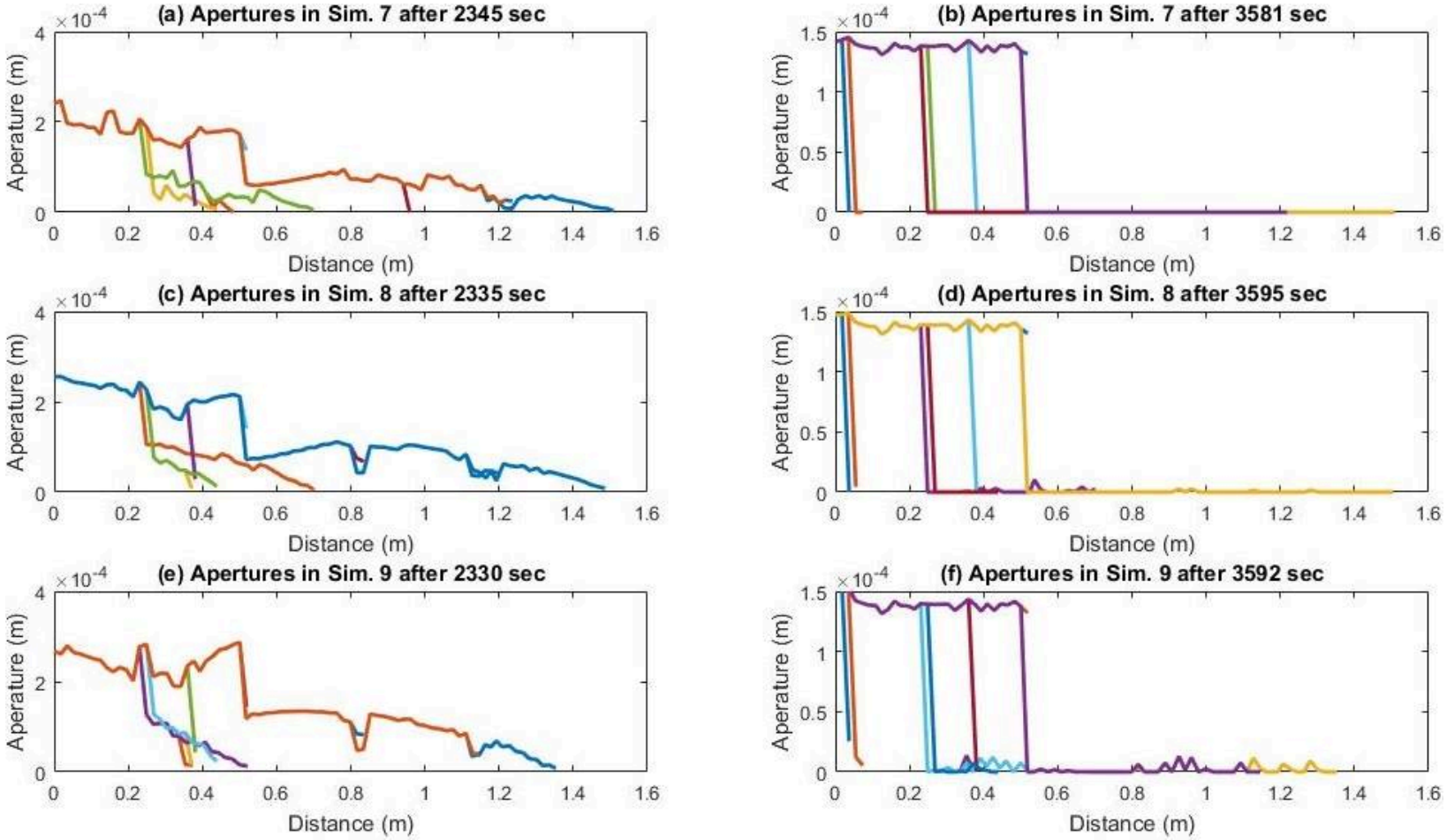

Figure 4.13. Hydraulic apertures in simulations with different fracture roughness. The left column is at end of injection, while the right column is some time after shut-in when the pressure has fallen below fracture closure pressure. Be aware that the values on the y-axis are different in the left and right column. Each fracture has its own color.

Hydraulic aperture of the fractures on the lower, right side of the borehole

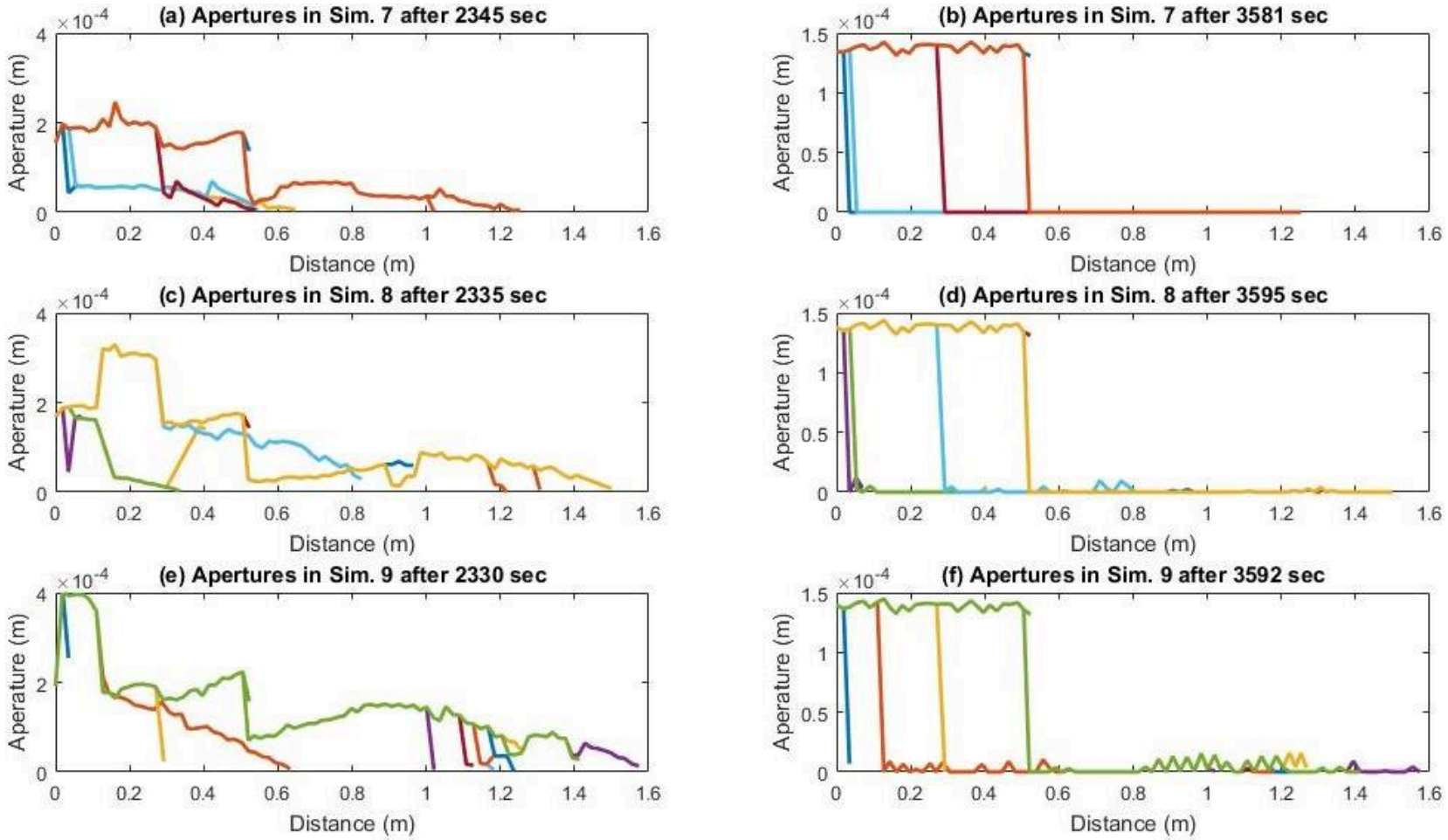

Figure 4.14. Hydraulic apertures in simulations with different fracture roughness. The left column is at end of injection, while the right column is some time after shut-in when the pressure has fallen below fracture closure pressure. Be aware that the values on the y-axis are different in the left and right column. Each fracture has its own color.

Permeability after fracture closure

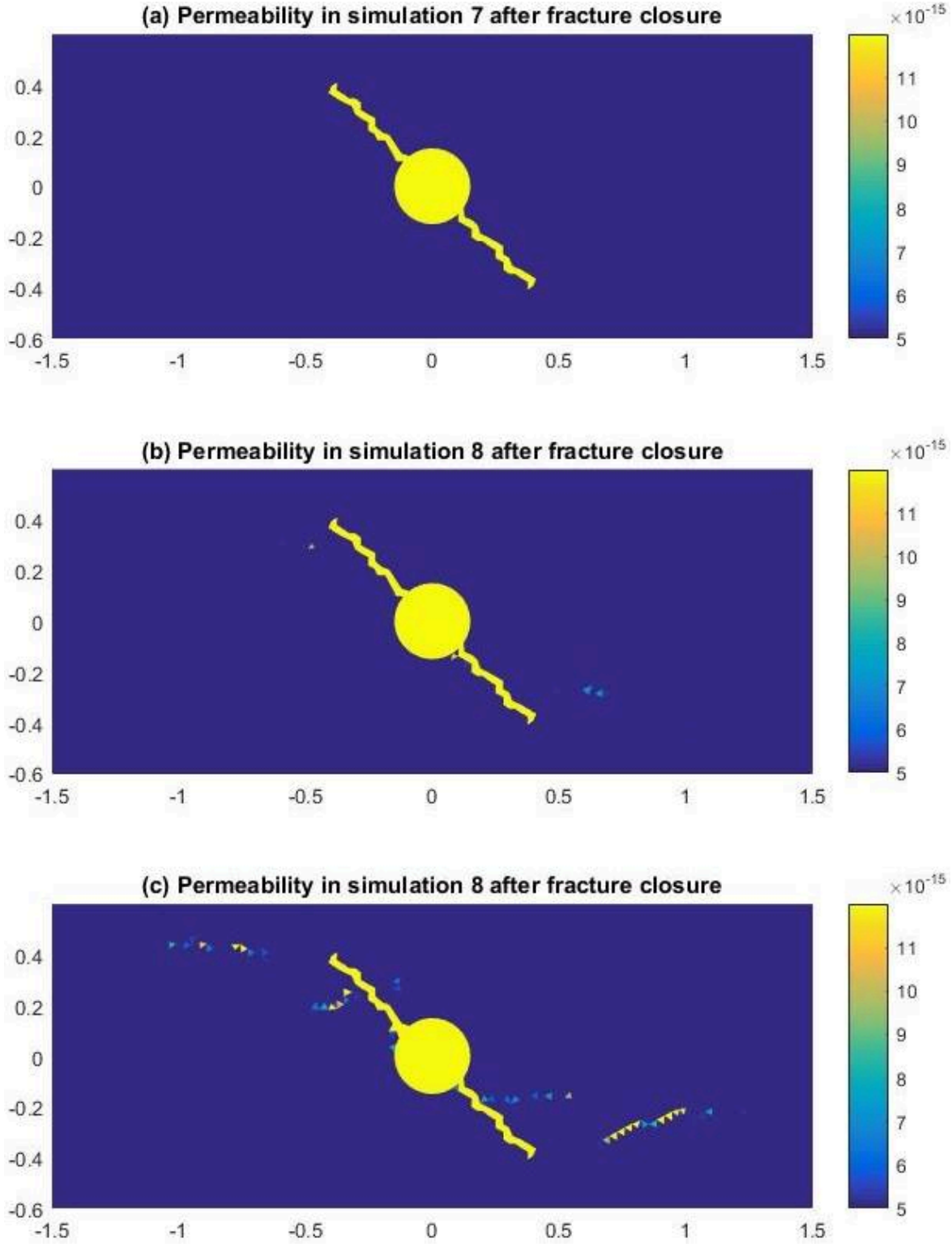

Figure 4.15. The remaining permeability after fracture closure. (a) is with smooth fracture walls. The asperities in (b) are 0.75 mm, and the asperities in (c) are 1.5 mm. The colorbar represents the permeability in square meters.

4.3.2 Discussion

Already in the figure showing the propagation patterns (Figure 4.10), the altered asperity heights show some kind of impact on the simulations. However, the important results are not seen in the fracture patterns, but in the fracture apertures after fracture closure. In Figure 4.11, increased apertures are seen, indicating shear displacement between the fracture walls during injection. As hoped, Figure 4.12 shows that some aperture is maintained also after fracture closure. Both the extent and the height of the remaining aperture increases with increasing asperity height. The graphs give a better understanding of the relative heights. In the right columns of the graphs, one sees how small the remaining apertures are in the induced fractures compared to the natural fracture. Based on Eq. 2.37, plotted in Figure 3.3, the remaining aperture in simulation 8 can potentially be 0.75 mm., while in simulation 9 it can be as large as 1.5 mm. The much smaller apertures seen after fracture closure (0.014 mm. at the most) indicate little final shear displacement. Nor the apertures seen at the end of injection change much between the simulations, especially when looking at the upper left side of the borehole (left column in Figure 4.13). The small shear displacement after fracture closure is thus not necessarily due to reduced shear displacement during fracture closure. It seems like the shear displacements during the entire treatment process is too small to release the full potential of shear-dilation. Another indicator of little shear displacement during injection is the propagation of a fracture in the opposite direction of all the others (in the middle of the upper, left natural fracture in all simulations). Based on the theory presented in Section 2.1.4, increased stresses due to shear displacement should hamper such propagation.

The ultimate goal of a fracture treatment is to enhance the permeability and increase the production. Figure 4.15 proves that shear-dilation creates additional permeability. Ideally, the effect could be more significant, but the results are encouraging; the shear displacement caused by increased fracture pressure is not completely reversed after the pressure is back to normal, i.e. shear-dilation can be used to create lasting permeability changes when fracture treatments are simulated. To increase the effect, a possible solution is to reduce u_*. As shown in Figure 4.16, the result will be larger dilation at small shear displacements. Based on theory (Dusseault, 2015: 63-65) increased shear displacement can be achieved by increasing the stress anisotropy.

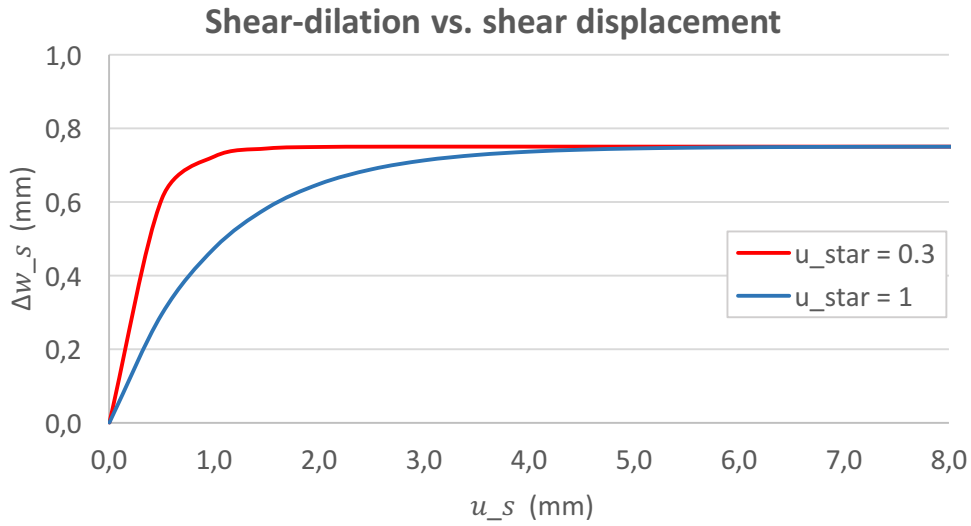

Figure 4.16. The effect of u_* on shear-dilation. $u_n = 0$ mm. The calculations are based on Eq. 2.37.

4.4 Altered viscosity of Newtonian fluids

4.4.1 Results

The two following figures focus on the propagation rate in simulations with different fluid viscosities. The fracture patterns are plotted at different times, and the colorbar represents pore pressure. The next two figures are basically the same plots, but a larger area of the reservoir is shown. In these two figures, the focus is the pore pressure distribution. Figure 4.21 shows the results of too low injection rate. The graphs in Figure 4.22 present the pressure profile in the main fractures in the two simulations.

Fracture propagation in simulation 4 with fluid viscosity of 1 cP

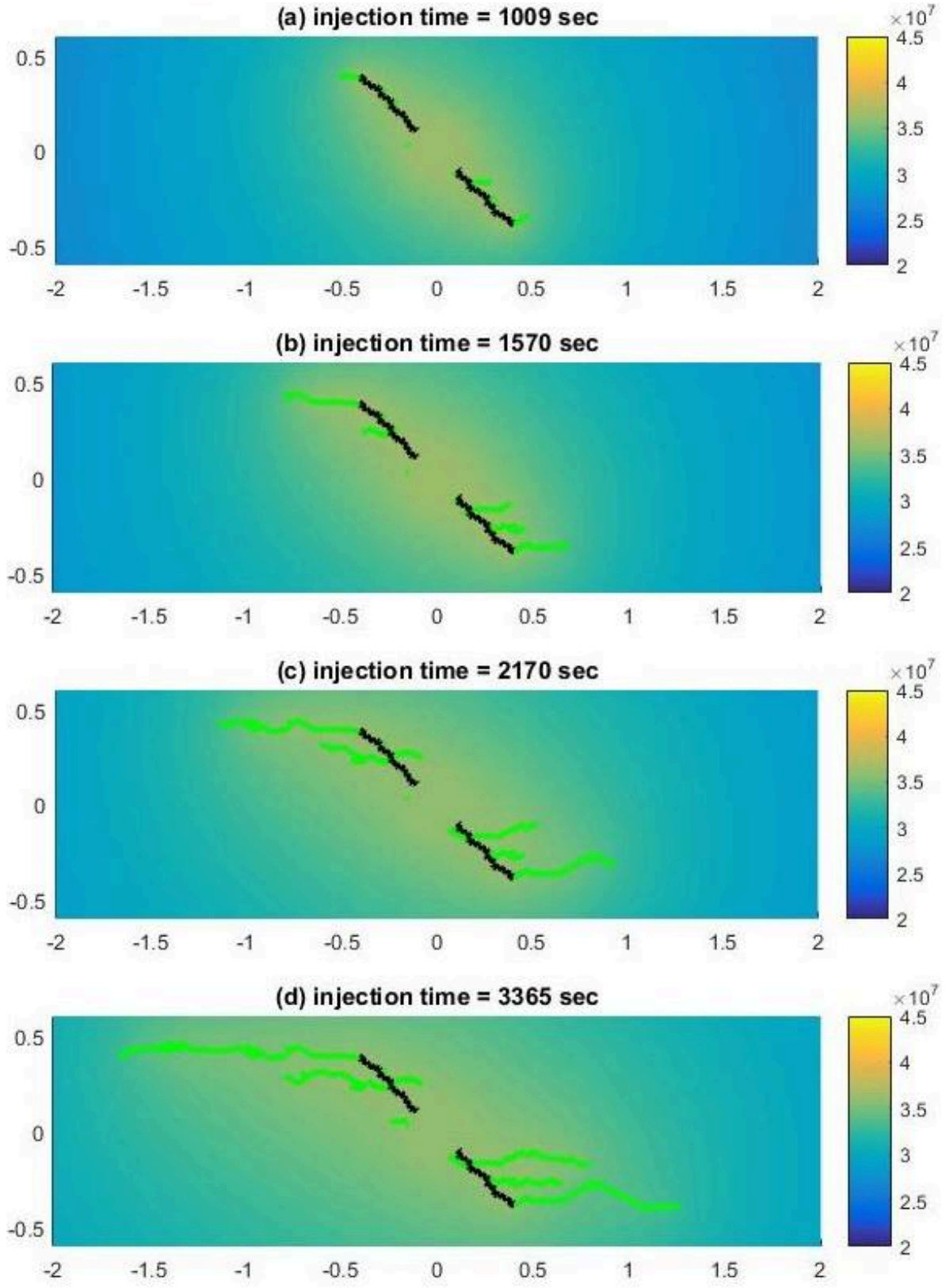

Figure 4.17. Fracture propagation with a fluid viscosity of 1 cP and an injection rate of 1.8 kg/s. The colorbar represents pore pressure.

Fracture propagation in simulation 10 with fluid viscosity of 2 cP

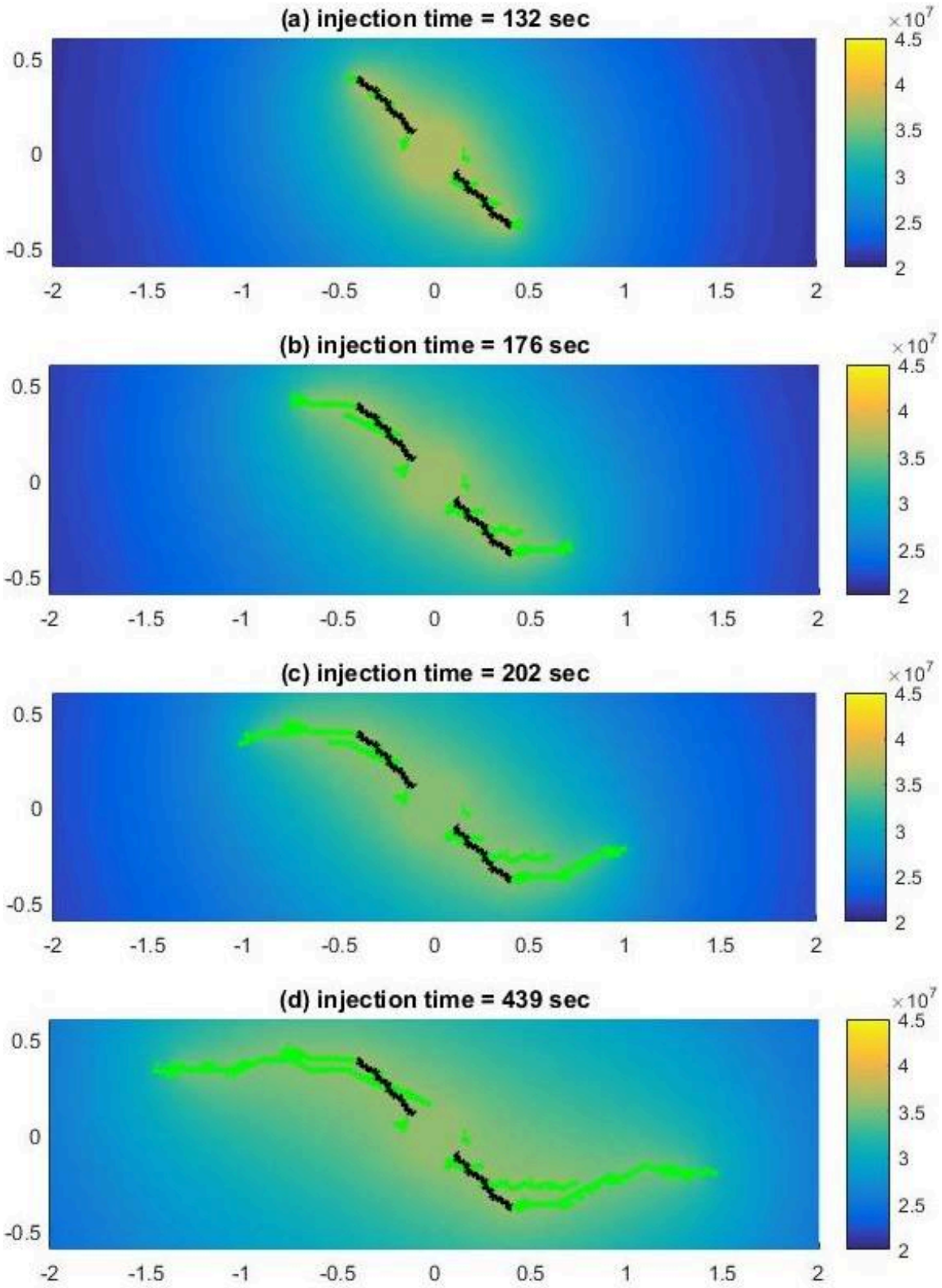

Figure 4.18. Fracture propagation with a fluid viscosity of 2 cP and an injection rate of 1.0 kg/s. The colorbar represents pore pressure.

Pore pressure distribution in simulation 4 with fluid viscosity of 1 cP

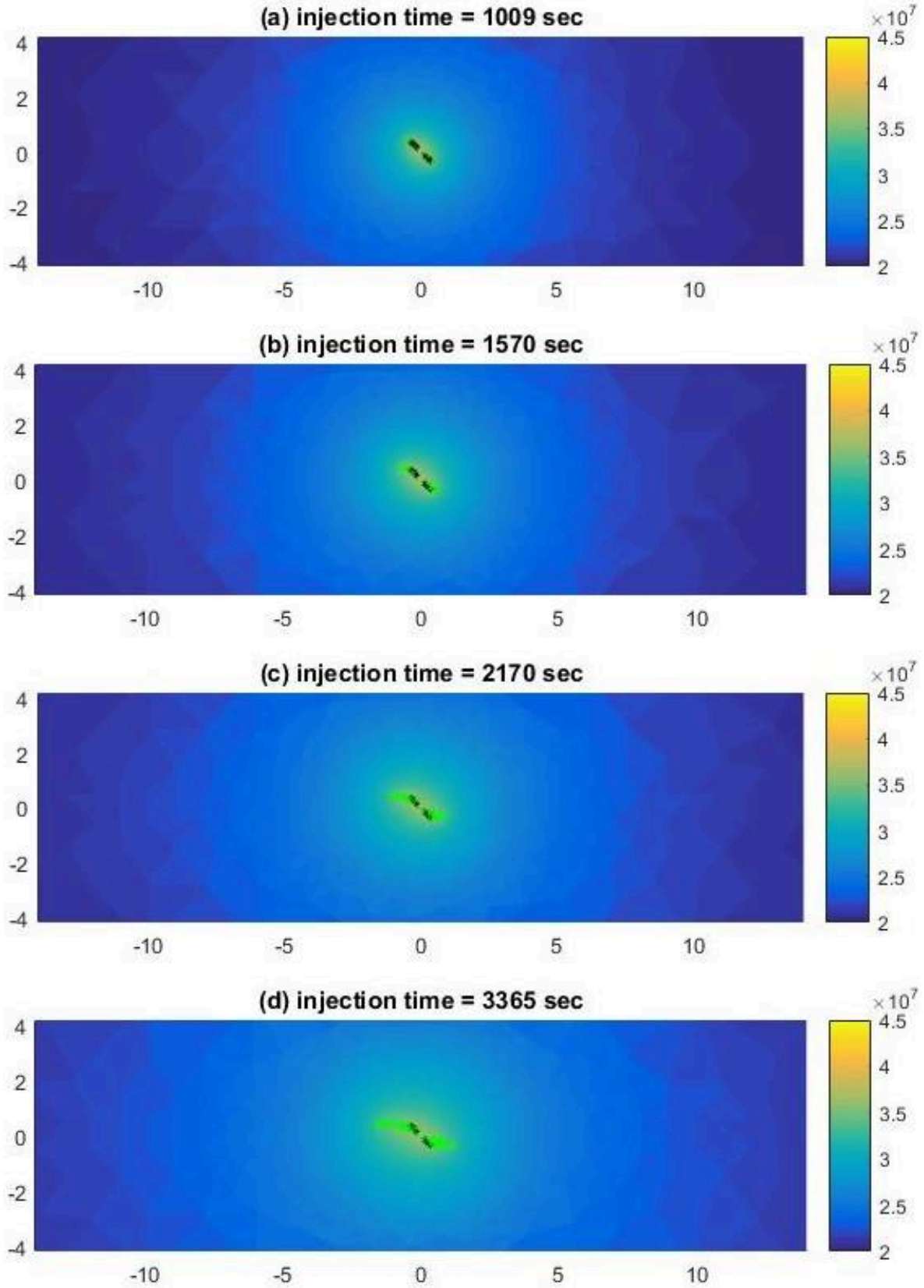

Figure 4.19. Pore pressure distribution with a fluid viscosity of 1 cP and an injection rate of 1.8 kg/s. The colorbar represents pore pressure.

Pore pressure distribution in simulation 10 with fluid viscosity of 2 cP

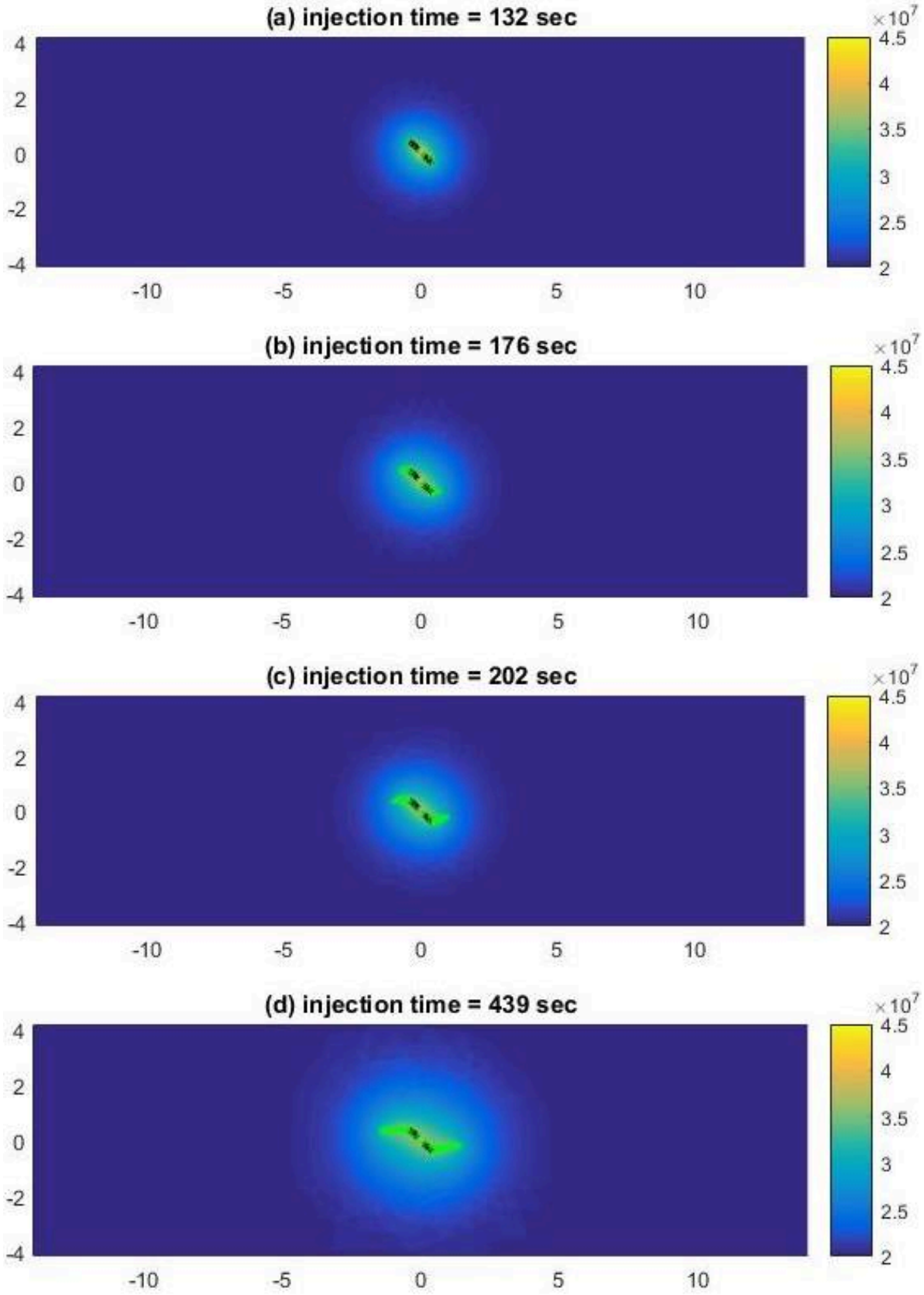

Figure 4.20. Pore pressure distribution with a fluid viscosity of 2 cP and an injection rate of 1.0 kg/s. The colorbar represents pore pressure.

Fracture propagation and pore pressure distribution with 1 kg/s water injection

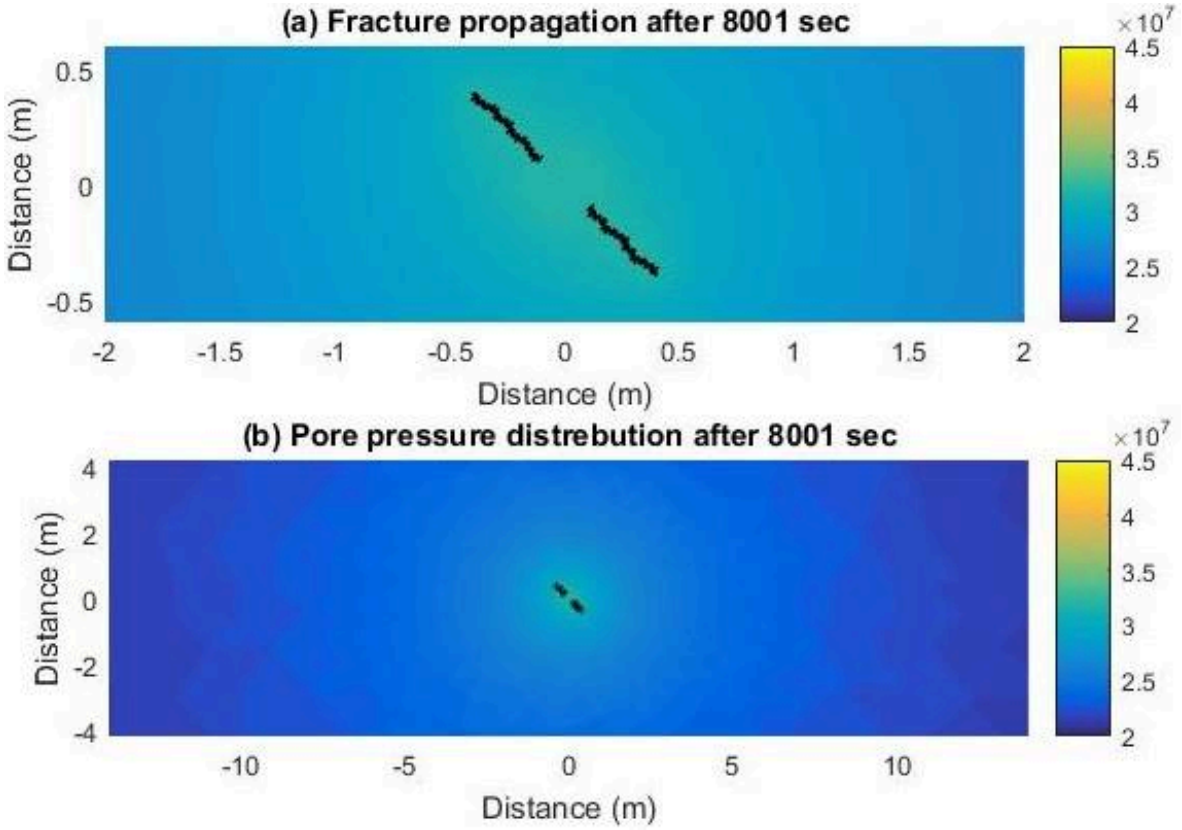

Figure 4.21. (a) Fracture propagation and (b) pore pressure distribution with a fluid viscosity of 1 cP and an injection rate of 1.0 kg/s after 8000 seconds. The colorbar represents pore pressure.

Fracture pressure in simulations with different viscosities

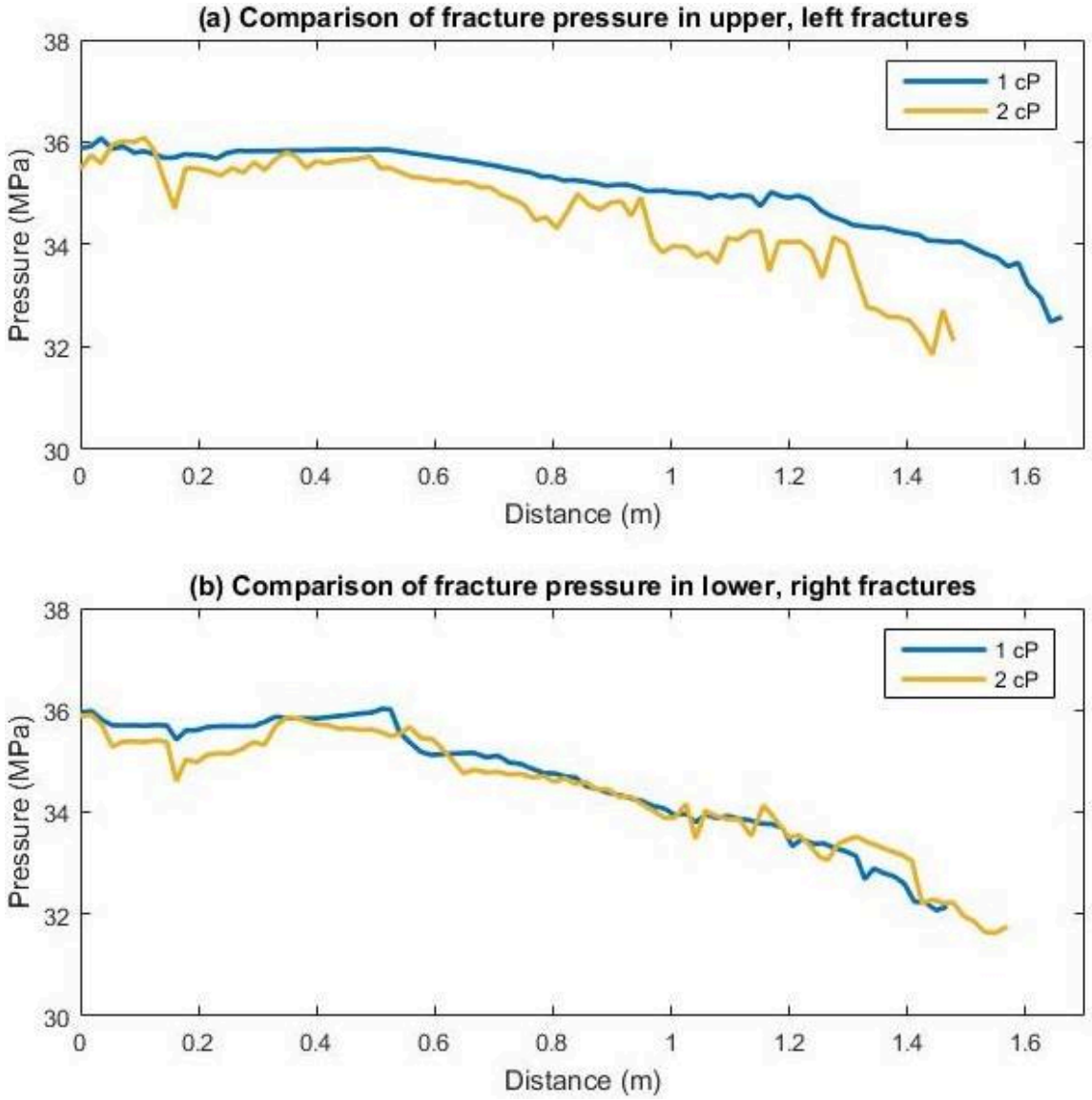

Figure 4.22. Comparison of fracture pressure in simulations done with different viscosities. Only the pressure in the main fracture is plotted. The blue lines are form simulation 4, and the yellow lines are from simulation 10.

4.4.2 Discussion

First of all, it is worth mentioning that the simulations conducted on altered viscosity do not fully represent the case where fracturing fluid viscosity is changed. Since a permeability change is used to mimic the altered viscosity, the whole formation is affected. That also includes reservoir fluids and their ability to dissipate pressure. The slightly odd event of sudden doubling of reservoir fluid viscosity makes it hard to find comparable literature on the topic. On the other hand, most flow equations are based on one, constant viscosity.

With that in mind, the results can be analyzed. The doubled fluid viscosity results in a significantly shorter time period before fractures are initiated, and then a significantly larger fracture propagation rate. During the simulated time period, every step of propagation takes almost ten times as long with the lower viscosity, and that includes a 1.8 times higher injection rate. 52 seconds and 52 kg of injected fluid were needed to initiate fracturing with a viscosity of 2 cP. With a viscosity of 1 cP, 346 seconds and 623 kg were needed. The differences might sound unrealistically big, but if one looks at the pressure profile in the whole reservoir it makes more sense. With the lower viscosity, especially since it applies to all the fluid in the reservoir, the increased pore pressure around the fractures dissipate further and faster into the formation. The effect can clearly be seen if Figure 4.19 and Figure 4.20 are compared. Figure 4.21b presents an even more extreme case where the formation manages to absorb all the injected fluid and spread it out into the formation. After injection of 8000 kg of water, fracture initiation still can't be seen.

The pressure profiles in the fractures do not vary much between the simulations (Figure 4.22). While the lower, right fractures have a more or less identical pressure profile, the upper, left fractures show some discrepancy. Viscosity is known to affect the pressure loss, but concurrently, so is flow rate. The viscosity difference in the two cases is a factor of two. The difference in flow rate is approximately the same. Based on Darcy's law, the differences should cancel:

$$\Delta P_2 = \frac{L(2\mu_1)q_1}{k} = \frac{L\mu_1(2q_1)}{k}. \qquad \text{Eq. 4.1}$$

Even though the simulations don't fully represent the reality, they clearly show the significant impact of fluid rheology and highlighted the need of changeable viscosity in MDEM.

5 Conclusion

The simulations have resulted in new or improved understanding of fracture mechanics and simulation challenges. The main takeaways are:

1. The presence and direction of natural fractures affect the half length of hydraulic fractures. To optimize well patterns and injection volumes, natural fractures must be taken into account.
2. Fracture propagation in natural fractures seems to be affected by pore pressure and irregularities. The grid effects of MDEM can be a good substitute for natural irregularities.
3. Shear-dilation in rough walled fractures can, to some extent, be used to simulate the effects of a fracture treatment. The mechanism is the same as experienced after water-fracs.
4. Changing the permeability of the reservoir to mimic an altered viscosity might work based on Darcy's law, but it will not reflect the reality. For the reservoir fluid viscosity to stay constant while the viscosity of the injected fluid is altered, improvements of the simulator are needed.

6 Further Work

The focus of this thesis was to compare MDEM and literature to get a better understanding of fracture mechanics. Some basic simulations have been conducted, but in the future more complex simulations are required. Below, further work is suggested to improve the results and increase the understanding of fracturing.

Natural fractures

New simulations should include several natural fractures spread out around in the formation to see if the hydraulic fracture still follows the findings of Maurice Dusseault (Dusseault, 2015), presented in Section 9 under "Fracture patterns".

Fall-off test

The time steps immediately after shut-in must be reduced to get a smoother and more accurate fall-off curve. Fall-off tests should be considered in less permeable formations where the pressure decrease is less rapid.

Shear-dilation

The simulations have shown promising results, but the effects seen so far are not sufficient to replace proppants. New simulations should be done with a reduced u_* to increase the effect of shear-dilation in simulations with little shear displacement. In an attempt to get more significant results, larger stress anisotropies should be applied in a naturally fractured formation.

Altered viscosity

The possibility of altering the viscosity of injected fluid, without altering the entire reservoir viscosity, should be implemented.

To fully utilize MDEM, also non-Newtonian rheologies must be implemented. Bingham plastic and power-law fluids are the most relevant to the petroleum industry.

7 Nomenclature

Abbreviations

DEM	Discrete Element Method
FDM	Finite Difference Method
FEM	Finite Element Method
JRC	Joint Roughness Coefficient
U.S.	United States
2D	Two-Dimensional
3D	Three-Dimensional

Parameters

$\boldsymbol{A}$	area
$\boldsymbol{a_{ij}}$	stiffness
$\boldsymbol{C}$	conventional constitutive matrix
$\boldsymbol{C_L}$	fluid-loss coefficient
$\boldsymbol{F}$	force
$\boldsymbol{f_n}$	normal contact force
$\boldsymbol{K}$	consistency index
$\boldsymbol{K}$	internal stiffness matrix
$\boldsymbol{k}$	permeability
$\boldsymbol{k_{ni}}$	normal stiffness of contact i
$\boldsymbol{L}$	length
$\boldsymbol{M}$	unit normal vector matrix
$\boldsymbol{P}$	pressure
$\boldsymbol{p_c}$	fracture closure pressure
$\boldsymbol{p_f}$	pore pressure
$\boldsymbol{p_{f0}}$	in-situ pore pressure
$\boldsymbol{p_w}$	well pressure
$\boldsymbol{p_{w,max}^{frac}}$	fracture pressure
$\boldsymbol{q}$	flow rate
$\boldsymbol{q_L}$	leak-off rate
$\boldsymbol{S_f}$	fracture stiffness
$\boldsymbol{T_0}$	tensile strength
$\boldsymbol{t}$	time

u	flow behavior index
U_n	normal relative displacement
u_n	normal displacement discontinuity
u_s	shear displacement discontinuity
u_*	scaling parameter
V	velocity
w	hydraulic aperture
$\bar{w}$	hydraulic fracture width
w_0	initial hydraulic aperture
$\Delta w_{(n)}$	change in hydraulic aperture from normal displacement
$\Delta w_{(s)}$	change in hydraulic aperture from shear displacement
α	tuning parameter
$\dot{\gamma}$	shear rate
ε	strain
η	poroelastic stress coefficient
θ	angle
λ	dimensionless scaling parameter
σ	stress
σ	standard deviation
σ'	effective stress
σ_v	vertical stress
σ_θ	tangential stress
τ	length of injection
τ	time of fracturing
τ	shear stress
μ	viscosity
μ_p	plastic viscosity

Units

cm	centimeter
cm^2	square centimeter
cP	centipoise
g	gram
GPa	gigapascal
kg	kilogram
MPa	megapascal
mm	millimeter

m^2	square meter
m^3	cubic meter
s	second
°	degrees

8 Bibliography

Alassi HT. (2008) Modelling Reservoir Geomechanics Using Descrete Element Method: Application to Reservoir Monitoring. *Petroleum Engineering and Applied Geophysics.* Trondheim: NTNU.

Alassi HT, Holt RM, Nes O-m, et al. (2011) Realistic Geomechanical Modeling of Hydraulic Fracturing in Fractured Reservoir Rock. *Canadian Unconventional Resources Conference.* Calgary, Canada: Society of Petroleum Engineers.

Barton N and Choubey V. (1977) The shear strength of rock joints in theory and practice. *Rock Mechanics* 10.

Bauer A. (2016) Hydraulic fracturing around injectors. Trondheim, Norway: SINTEF Petroleum Research.

Bourgoyne Jr. AT, Millheim KK, Chenevert ME, et al. (1986) *Applied Drilling Engineering*: SPE Textbook Series.

Bruni MS and Nakagawa FM. (1991) Pore Pressure Influence on Tensile Fracture Propagation in Sedimentary Rock. *Int. J. Rock Mech. Min. Sci. & Geomech.* 28: 261-273.

Clark JB. (1949) A Hydraulic Process for Increasing the Productivity of Wells.

Cleary MP. (1979) Rate And Structure Sensitivity In Hydraulic Fracturing Of Fluid-Saturated Porous Formations. *American Rock Mechanics Association.* Austin, Texas: American Rock Mechanics Association.

Dusseault MB. (1989) Behavior of Induced Fractures in Sans and Friable Sandstones. *Journal of Hydrology*.

Dusseault MB. (2015) Geomechanics in Shale Gas Development. *Geotechnical Synergy in Buenos Aires 2015.* IOS Press.

Egan M. (2016) *Oil milestone: Fracking fuels half of U.S. output*. Available at: http://money.cnn.com/2016/03/24/investing/fracking-shale-oil-boom/.

Fjær E, Holt RM, Horsrud P, et al. (2008) *Petroleum related rock mechanics*: Elsevier.

Geilikman M, Xu G and Wong S-W. (2013) Interaction of Multiple Hydraulic Fractures in Horizontal Wells. *SPE Unconventional Gas Conference and Exhibition.* Muscat, Oman: Society of Petroleum Engineers.

Guo J and Liu Y. (2014) Numerical Simulation of Hydraulic Fracture Crossing Natural Fracture at Orthogonal Angles. *The Electronic Journal of Geotechnical Engineering* 19.

Hopkin EA. (1967) Factors Affecting Cuttings Removal During Rotary Drilling. *Journal of Petroleum Technology* 19.

Howard GC and Fast CR. (1957) Optimum Fluid Characteristics for Fracture Extension. American Petroleum Institute.

Lavrov A, Larsen I and Bauer A. (2016) Coupling a fracture code to a transient reservoir simulator: a hands-on approach. *US Rock Mechanics / Geomechanics Symposium.* Houston, Texas: American Rock Mechanics Association.

Marongiu-Porcu M, Ehlig-Economides CA and Economides MJ. (2011) Global Model for Fracture Falloff Analysis. *North American Unconventional Gas Conference and Exhibition.* The Woodlands, Texas: Society of Petroleum Engineers.

Mayerhofer MJ, Richardson MF, Walker RN, Jr., et al. (1997) Proppants? We Don't Need No Proppants. *SPE Annual Technical Conference and Exhibition.* San Antonia, Texas: Society of Petroleum Engineers.

Mehrishal A and Sharifzadeh M. (2012) Evaluation of Rock Joint Hydraulic Aperture using Wavelet Theory. International Society for Rock Mechanics.

Mitani Y, Sharifzadeh M, Esaki T, et al. (2005) Development of Shear-flow Test Apparatus And Determination of Coupled Properties of Rock Joint. International Society for Rock Mechanics.

Morton MQ. (2013) Unlocking the Earth - A Short History of Hydraulic Fracturing. *GEOExPro.*

Newendorp PD and Menzie DE. (1965) Analysis Of Fracture Treatment Pressure Fall-Off Data. *SPE Permian Basin Oil Recovery Conference.* Midland, Texas: Society of Petroleum Engineers.

Nolte KG. (1979) Determination Of Fracture Parameters From Fracturing Pressure Decline. *SPE Annual Technical Conference and Exhibition.* Las Vegas, Nevada: Society of Petroleum Engineers.

Nolte KG. (1986) A General Analysis of Fracturing Pressure Decline With Application to Three Models.

Nolte KG. (1988) Principles for Fracture Design Based on Pressure Analysis.

Nowak TJ and Lester GW. (1954) Analysis of Pressure Fall-Off Curves Obtained in Water Injection Wells To Determine Injective Capacity and Formation Damage. Society of Petroleum Engineers.

Odling NE. (1997) Fluid flow in fractured rocks at shallow levels in the Earth's crust: an overview. In: Holness MB (ed) *Deformation-enhanced fluid transport in the Earth's crust and mantel.* London: Chapman & Hall.

Palisch TT, Vincent MC and Handren PJ. (2008) Slickwater Fracturing: Food for Thought. *SPE Annual Technical Conference and Exhibition.* Denver, Colerado: Society of Petroleum Engineers.

Rongved M. (2015) Hydraulic Fracturing of Enhanced Geothermal Systems. *Department of Petroleum Engineering and Applied Geoscience.* NTNU.

Saboo N and Kumar P. (2016) Use of flow properties for rheological modeling of bitumen. *International Journal of Pavement Research and Technology* 9.

Schein G. (2005) The Application and Technology of Slickwater Fracturing. Society of Petroleum Engineers.

Shapiro SA. (2015) *Fluid-Induced Seismicity*: Cambridge University Press.

Smith MB and Shlyapobersky JW. (2000) Reservoir Stimulation. 3 ed.: Wiley.

Tse R and Cruden DM. (1979) Estimating Joint Roughness Coefficients. *International Journal of Rock Mechanics and Mining Science* 16.

Valko P and Economides MJ. (1997) Fluid Leakoff Delineation in High-Permeability Fracturing. *SPE Production Operations Symposium.* Oklahoma City: Society of Petroleum Engineers.

Walker RN, Jr., Hunter JL, Brake AC, et al. (1998) Proppants, We Still Don't Need No Proppants - A Perspective of Several Operators. *SPE Annual Technical Conference and Exhibition.* New Orleans, Louisiana: Society of Petroleum Engineers.